ISTITUTO NAZIONALE DI FISICA NUCLEARE

Sezione di Napoli

INFN/AE-94/08
18 Febbraio 1994

B. D'Ettorre Piazzoli, G. Di Sciascio:

MONTECARLO SIMULATION OF PHOTON-INDUCED AIR SHOWERS

To be published in Astroparticle Physics

Servizio Documentazione
dei Laboratori Nazionali di Frascati

INFN – Istituto Nazionale di Fisica Nucleare
Sezione di Napoli

INFN/AE–94/07
18 Febbraio 1994

MonteCarlo simulation of photon-induced air showers

B. D'Ettorre Piazzoli, G. Di Sciascio

Dipartimento di Scienze Fisiche dell'Università di Napoli and
Istituto Nazionale di Fisica Nucleare, sez. di Napoli, Italy

Abstract

The EPAS code (Electron Photon-induced Air Showers) is a three-dimensional MonteCarlo simulation developed to study the properties of extensive air showers (EAS) generated by the interaction of high energy photons (or electrons) in the atmosphere. Results of the present simulation concern the longitudinal, lateral, temporal and angular distributions of electrons in atmospheric cascades initiated by photons of energies up to $10^3\,TeV$.

1. INTRODUCTION

Interest in air shower studies has been pushed up by the discovery of high energy γ-rays from peculiar astrophysical objects such as pulsars or binary systems. As a consequence, in recent years very large arrays devoted to the detection of γ-initiated air showers have been constructed or planned all over the world.

Air shower experiments searching for ultra high energy gamma sources must distinguish showers initiated by gammas from those produced by primary cosmic rays. This fact highlights the need for detailed calculations of the shower development to get

an accurate description of the basic properties of the atmospheric cascade in order to identify measurable variables in which the gamma and hadronic showers are different.

Several authors have carried out calculations of electromagnetic cascades induced by the interaction of high energy photons or electrons. For high primary energies analytical and numerical calculations have been developed in order to save computing time, and various semplifications and approximations in describing the elementary processes have been adopted. However, the analytical and numerical approaches are suitable only for obtaining an average picture of the cascade shower [1].

Alternatively, Monte Carlo simulations under Approximation B [2] (asymptotic cross section of breemsstrahlung and pair production processes and constant ionisation energy loss of electrons) or hybrid MonteCarlo programs obtained folding existing simulation codes [3] have been developed. Other methods used to decrease the computing time include the "thin sampling" procedure and the "tail method" proposed by Hillas [4] and the technique of sampling the particle scattering only at the observation point and not at intermediate points along the path [5]. Such approximation procedures may introduce some degree of inaccuracy not easy to assess and may lead to results which have substantial discrepancies and are difficult to compare each other.

To meet the lack of detailed simulations of γ-ray initiated air showers we have developed a full three-dimensional Monte Carlo simulation of electron or photon induced air showers (EPAS) applicable even in the extremely high energy region. EPAS has been developed with the aim of building a multipurpose package covering the EAS physics [a Monte Carlo simulation of hadronic cascades (HEMAS) has been recently developed [6]]. The merit of a precise code is of providing results which do not suffer from difficulties inherent either in conventional cascade theory, due to the application of asymptotic cross sections, or in Monte Carlo simulations using approximate procedures. They can be used as a reference to set the degrees of accuracy of solutions to the cascade problems obtained by means of other methods.

The present paper is concerned with the properties of the electromagnetic component of air showers initiated by photons of energy up to $10^3\ TeV$. Simulations were carried out to provide the longitudinal development, the energy spectra, the angular and temporal distributions of both electrons and photons at different stages of the cascade development. Most of the results at the highest energies has been obtained for the atmospheric depth of 800 g/cm^2 corresponding to the altitude of the EAS-TOP [7] experiment. Great care has been taken to gather information about fluctuations. Accounting for fluctuations from shower to shower is essential in calculating effective areas and temporal resolutions of EAS arrays. Shower photons, to which not much attention was paid till now, have been included because they can contribute, by means of the Rossi transition effect, to the formation of the signal in the plastic scintillators, usually housed in a thin steel box. However, results concerning the photon component will be presented in a separate paper. EPAS follows electrons and photons down to the $2\,MeV$ range. The structure of the code allows for including the production of Cerenkov radiation. However in the present version this process has been not taken into account.

Hadronic interactions of photons and inelastic electron-nucleus interactions are included in the general scheme of the code, but in the present version these interactions are switched off and the calculation of the hadronic cascade is not carried out. That does not spoil the accuracy of the calculations concernig the pure electro-photon cascade which, due to the relevant difference between the electromagnetic and hadronic cross sections of photons (electrons), can be followed without coupling to hadron cascade calculations. Moreover, in order to keep generality and allow for comparison with other calculations, the geomagnetic effect is not taken in to account, although electrons and positrons are followed separately.

In sect. 2 the elementary processes involved in the simulation are summarized and the treatment of Coulomb scattering discussed. The results are given in sect. 3 .

2. ELEMENTARY PROCESSES

The following processes are included in the simulation:

i) energy dependent pair production and bremsstrahlung cross sections, accounting for an accurate description of the screening effect [8] (Fig. 1). The angular distribution of electrons and photons radiated in these processes are accounted for according to the Sommerfeld's formula [9]. Bremsstrahlung photons below a cut-off energy are not generated and their production is included as a continuous energy loss;

ii) Compton effect [10];

iii) photoelectric effect [11];

iv) production of knock-on electrons above a cut-off energy by electrons and positrons (Moller and Bhabha scattering respectively [12]). Energy losses involving transfers less than this cut-off are accounted for by means of the appropriate expressions for the restricted mean collision-loss [13] (Fig. 2);

v) annihilation in flight of positrons [14];

vi) multiple Coulomb scattering of electrons; this process has been carefully investigated since it provides the main contribution to the displacement of charged particles from the shower axis. So, if one is dealing with an electron (or positron), continuous energy losses and Coulomb scattering along each track segment have to be sampled.

Two methods have been implemented: the Moliere theory corrected for finite angle scattering ($\sin\theta \neq \theta$) as described by Bethe [15] and the gaussian approximation. In Fig. 3 the differential scattering distributions obtained in the gaussian approximation using the mean scattering angles proposed by different authors [1, 15, 16, 17] are compared to the prediction of the Moliere theory. The Highland parametrization [16] gives the best

overall agreement with Moliere theory. The use of the Highland parametrization with a new set of constants as proposed by Lynch and Dahl [18] does not affect the result.

A path length correction has been included to take into account the increase in path length over the straight line distance due to multiple scattering [19]. Moreover we allow for the change in energy due to continuous energy losses (ionization and soft photon radiation) by replacing E^2 by E_0E, β^2 by $\beta_0\beta$, etc., in the expression for $\sqrt{<\theta^2>}$, where E_0 and β_0 are the initial and E and β the final energies and velocities respectively [20].

A source of error results from the assumption that all the scattering takes place at the end of the track segment. This can be minimized by keeping the maximum step length short enough at low energies where scattering is greatest. Thus, if the mean scattering angle corresponding to the actual path length is greater than a limit value θ_m the path has been subdivided into a number of sub-steps in order to satisfy this requirement. We moved θ_m between 2 and 10 degrees and found very negligible differences. A good compromise between computing time and accuracy suggests $\theta_m = 4^0$. Irrespective of the method of sampling the scattering angle, the correlation between the deviation of the particle position and the corresponding angular deviation has been taken into account in the gaussian approximation [1].

The lateral distribution of the electron component of $1\,TeV$ photon-initiated showers with $E = 5\,MeV$ electron threshold energy is shown in Fig. 4. Crossed points are obtained using gaussian approximation with the Highland mean scattering angle, diamonds refer to the Moliere theory. A satisfactory agreement is found in the important range of radial distances from the shower axis. Further checks for different primary energies, depths and electron cut-off energies have confirmed the possibility of using the gaussian approximation without affecting the accuracy of results. The reason is that the main contribution to the lateral spread is due to the multiple scattering of many low energy particles, a process of high probability as compared to the large angle scattering of energetic electrons. The use of the gaussian approximation allows a reduction of computing time at least of a factor of two.

3. RESULTS

Present simulations concern the development of electron-photon cascades in the U.S. standard atmosphere generated by vertical primary photons of $0.1, 1, 10, 10^2, 10^3\ TeV$ energy (5000, 5000, 1000, 100, 100 cascades respectively). Results concerning the electron component are presented. The electrons are followed up to a threshold energy E_{th} of 5 MeV. The radiation length of air was taken to be 37.1 g/cm^2, the critical energy $\epsilon_0 = 81\ MeV$.

3.1 Longitudinal development

The longitudinal development of the electron component is shown in Fig. 5 . The average number of electrons at a depth t (measured in radiation lengths) $\overline{N}_e(E_0, E_{th}, t)$, where E_0 is the energy of the primary photon, is well described by a modified form of the Greisen formula [21]

$$\overline{N}_e(E_0, E_{th}, t) = A_e(E_{th}) \frac{0.31}{\sqrt{y}} exp[t_1(1 - 1.5\ ln\ s_1)] \tag{1}$$

where $A_e(E_{th})$ is the fraction of electrons having energies larger than E_{th} as compared to the total number of electrons, $y = ln(E_0/\epsilon_0)$ and t_1 is the modified depth according to the expression

$$t_1 = t + a_e(E_{th}) \tag{2}$$

where $a_e(E_{th})$ is a threshold energy-dependent parameter.

The shower age s_1 is calculated using the modified t_1 value

$$s_1 = \frac{3t_1}{t_1 + 2y} \tag{3}$$

The $A_e(E_{th})$ and $a_e(E_{th})$ values, given in table I for $0.1 \leq E_0 \leq 10^3 TeV$ and $2 < t < 24$, can be interpolated for intermediate E_{th} values with a reasonable accuracy. We find a satisfactory agreement with the results of the simulations carried out by Fenyves et al. [22] at energies up to $10\ TeV$.

3.2 Fluctuations

The dispersion

$$\sigma_d = \left[\frac{1}{n-1}\sum_{i=1}^{n}(N_{e_i} - \overline{N}_e)^2\right]^{1/2} \tag{4}$$

around the average value is attached to the transition curves in Fig. 6. The distribution of the electron number around the average value follows a rather complicated evolution. Minimum dispersion occurs near the depth of the shower maximum, as shown in Fig. 7, with values larger than expected according to a Poisson distribution. For many depth units after the maximum - which is the usual experimental condition - the size distribution for a fixed primary energy acquires a positive skewness.

We find that in the whole energy range here explored ($0.1 \div 10^3\ TeV$) and in the age range $0.9 \leq s_1 \leq 1.6$ (at least), the size ($E_{th} = 5\ MeV$) fluctuates according to a log-normal distribution

$$f(N_e)dN_e = \frac{K}{C}\frac{1}{\sqrt{2\pi}\sigma_{10}}\frac{1}{N_e}exp\left[-\frac{(log_{10}N_e - \mu_{10})^2}{2\sigma_{10}^2}\right]dN_e \tag{5}$$

where $C = ln\ 10$, $1 \leq N_e \leq \infty$ and

$$K = \frac{2}{1 + erf(\mu_{10}/\sigma_{10}\sqrt{2})}. \tag{6}$$

The parameter $K = 1$ for any practical purpose. The size distribution given by formula (5) is normalized to the unity so that

$$\overline{N}_e = \int N_e \cdot f(N_e) dN_e. \tag{7}$$

To check the goodness of this representation we can exploit the relation between $\overline{N}_e$ (the Greisen value) and the parameters μ_{10} and σ_{10}

$$\mu_{10} = log_{10}\overline{N_e} - \frac{C}{2}\sigma_{10}^2 \tag{8}$$

A two-parameter fit to the electron distribution using (5) provides the best values for μ_{10} and σ_{10} and, throughout (8), an average size $\overline{N_e}(\mu_{10}, \sigma_{10})$, which is compared in Fig. 8 to the Greisen value $\overline{N}_e$. The agreement is excellent. The dependence of μ_{10} on energy E_0 and age s_1 can be parametrized by means of a twofold parabolic form $\mu_{10}(y, s_1) = \sum_{i,j} b_{ij} y^i s_1^j$ $(i, j = 0, 1, 2)$ with

$$b_{ij} = \begin{pmatrix} 1.1233 & -3.4872 & 1.5204 \\ -0.7749 & 2.1270 & -0.9628 \\ 0.0457 & -0.0773 & 0.0329 \end{pmatrix}$$

From formula (8) the standard deviation σ_{10} can be obtained. The log-normal distribution reproduces very nicely the MonteCarlo results as shown in Fig. 9.

3.3 The energy spectrum

The integral energy spectrum of electrons for different energies and depths is shown in Fig. 10 . The formula given by Hillas [23] provides a good representation up to electron energies of 50 MeV. The energy spectrum, normalized at 5 MeV, agrees well with the calculations of Richards and Nordheim [24] at $s_1 = 1$ (Fig. 11).

3.4 The lateral distribution

The evaluation of the lateral spread of electrons is essential for determining the shower parameters from experimental data. The validity of the Nishimura-Kamata-Greisen (NKG) formula [17] with a single age parameter has been questioned since the measured radial electron distributions are found steeper than the expectations based on this function. A slight increase of the age parameter with distance r from the shower axis has been proposed in order to fit the radial distribution at any point using the NKG formula [25].

Alternatively, from MonteCarlo simulations below $0.1\,TeV$ Hillas suggested the use of the NKG formula with constant age parameter but with about one-half of the Moliere length [26]. This has been checked by Fenyves et al. [22] up to $10\,TeV$ at the depth of 850 g/cm^2. Our simulations extend the validity of the Hillas parametrization up to $10^3\,TeV$ in the age range $0.4 \div 1.6$ when a modified value of the age parameter

$$s_2 = \frac{3t_2}{t_2 + 2y} \tag{9}$$

is adopted. Here $t_2 = t + b_e(E_{th})$ with the parameter $b_e(E_{th})$ depending on the electron threshold energy. At $E_{th} = 5\,MeV$ it is -0.44. We note that the age parameter s_2 of the lateral development is smaller than the s_1 values used to describe the longitudinal development of the shower.

The normalized lateral density distribution of the electron component of photon-initiated showers is shown (crossed points) in Fig. 12 for different primary energies ($0.1\,TeV \div 10^2\,TeV$) and different depths. The reported points refer to the function $\rho_e(r) = \frac{\Delta_e(r)}{N_e}$ where N_e is the total number of electrons, r the distance from the shower axis, and $\Delta_e(r)$ the local density of electrons. MonteCarlo data are well represented by the function $\frac{1}{r'^2_M} f(r/r'_M)$, where $f(r/r'_M)$ is the modified NKG formula:

$$f\left(\frac{r}{r'_M}, s_2, E_0\right) = C(s_2)\left[\frac{r}{r'_M}\right]^{s_2-2}\left[\frac{r}{r'_M}+1\right]^{s_2-4.5}. \qquad (10)$$

Here $r'_M = r_M/2$, r_M = Moliere length ($r_M = 90\ m$ at $850\ g/cm^2$), and s_2 is the modified age parameter. The distributions obtained via the original NKG formula look considerably flatter as shown in Fig. 13 .

On the contrary, the lateral distribution of the photons agrees very well with the original NKG formula, as shown in Fig. 14. This results confirms that photons are spread farther from the shower core than the electron, a consequence of the fact that photons do not lose energy by ionization and can travel at larger distances than electrons. This effect could explain the experimental ambiguity concerning the lateral distribution of charged particles if a local conversion of photons is allowed.

It has been remarked, however, that if r_M and s_2 are treated as free parameters, a large set of these values could provide a good representation of the lateral distribution [27]. In Fig. 15 curves corresponding to the NKG function calculated for different couples (r_M, s_2) are superimposed to the Monte Carlo results ($E_0 = 10^3 TeV, 800 g/cm^2$). The agreement is equally satisfactory for r_M values ranging from 10 to 100 m.

In a real experiment where the measurements are affected by experimental errors, different solutions could appear equivalent. Thus, due to the strong correlation between r_M and s_2, the determination of the age parameter depends heavily on the r_M value adopted.

3.5 Time structure

The measurement of time delays of charged particles makes it possible to estimate the direction of air showers. Consequently, the determination of the shape of the shower front is of great importance for γ-astronomy, where a good accuracy in the determination of the arrival direction is required.

Near the core charged particles form, as a first approximation, a plane disc. At great distances from the core the shower front takes the form of a spherical surface. Hence, even in the case of vertical incidence the particle arrivals are not simultaneous. The exact shape of the shower front should be taken into account when arrival times of particles which have been recorded far from the shower core are used to reconstruct the arrival direction.

Data on the arrival-time distribution of shower particles concern hadronic showers, but most of delay near center comes from spread in the electromagnetic component. The experimental information is still scant but enough to derive a disk thickness equivalent to $4 \div 8\ ns$ near the core, but rapidly increasing with distance. In fact the thickness is determined by the mean scatter of the trajectory lengths of the shower particles at the observation plane: a few meters within $10\ m$ from the axis, tens to hundreds of meters at much greater distances where the shower diffuses rapidly. Thus the particle arrivals exhibit a time spread increasing with the distance from the shower axis (we note, however, that at large r muons produced in hadronic showers are also important in defining shower thickness).

As an illustration we show the time distribution of the electron component of $10^2 TeV$ photon initiated showers as a function of the core distance, Fig. 16 (depth $800\ g/cm^2$, $s_1 = 1.3$). The time delay is calculated relative to the arrival time of a photon moving along the primary direction. The time delay distribution has a very sharp early peak (a few ns) near the core ($r < 10\ m$). At greater distances the spread increases noticeably, and particles delayed by more than $30\ ns$ are present.

The average particle delay $< t >$ and the full width at half maximum (a measure of the shower thickness) are shown in Fig. 17 for $10^2 TeV$ photon showers at different stages of the longitudinal development ($s_1 = 0.7, 1, 1.4$). At close distances from the shower axis ($r < 30\ m$) the slope $d < t > /dr$ does not depend on the age. At larger distances the slope exhibits a slight decrease with s_1. This merely reflects a geometric effect

because at a fixed core distance the increase of the observational level in atmosphere determines the sampling of particles trajectories with decreasing angles relative to the shower axis.

In Fig. 18 the average delay as a function of the core distance is shown for different primary energies at the values $s_1 = 0.7, 1.0, 1.4$. We notice that for $s_1 \geq 1$ the shower time profile is practically independent of the energy. It assumes a conical shape with a slope $d < t > /dr$ of about $0.17 ns/m$ and $0.14 ns/m$ at $s_1 = 1$ and $s_1 = 1.4$ respectively.

In most experiments only the arrival time of the first particle t_1 passing through the detectors is measured and used for fast timing purposes. The distribution of t_1 as a function of core distance is shown in Fig. 19 for $E = 10^2\ TeV$, $s_1 = 1.4$. The mean time delay of the first particle $< t_1 >$ (averaged on many showers) is plotted in Fig. 20 for different photon energies and age parameters. These plots confirm that near the core the geometrical shower front forms a plane disc whose radius increases with increasing energy. However, these figures show that $< t_1 >$ does not have the same behaviour as $< t >$ for the dependence on the radial distance from the shower axis. In fact, the shower time profile provided by $< t_1 >$ exhibits a parabolic shape which clearly depends on energy.

Though time fluctuations in high energy showers appear rather small, they have to be properly considered if a good accuracy in the reconstruction of the arrival direction by fast timing is required. We notice that the previous distributions have been obtained by integrating the time information over a ring at distance r. In a real experiment we can expect a contribution from sampling fluctuations due to the finite size of the detector. A preliminary study [28] shows that small area detectors ($\sim 1 m^2$) provide a 'picture' of the shower front not so flat as expected according to the distributions of Fig. 20. This effect is shown in Fig. 21 where the integral time delay distribution of the first electron recorded by increasing size detectors placed at 50 m from the shower core is reported for two gamma energies (10^2 and $10^3\ TeV$). The time distribution of the first electron

hitting at distances between 45 and 55 m from the core is shown for comparison. Final results of this investigation will be presented elsewhere.

3.6 Angular distribution of shower electrons

An alternative technique to the fast timing method has been proposed by Poirier et al. [29] who explored the possibility of finding the direction of the primary particle by measuring the angles of the shower electrons at the detection level. According to their calculations an accuracy of the order of $1/4^0$ could be achieved from the measurement (at sea level) of the directions of $> 10\ MeV$ electrons generated by primary photons of $10^2\ TeV$.

In this investigation it is convenient to use as angular variables the projections onto two orthogonal planes of the angle between the electron direction and that of the primary photon. Thus following Ref. [29] we define θ_R as the track angle projected onto the z-r plane and θ_T as the track angle projected onto a plane orthogonal to the z-r plane (z identifies the primary direction, r is the outward radial direction).

The angular distributions of θ_R and θ_T are plotted in Fig. 22 for two examples of radial distances from the shower core, $0 < r < 10\ m$ and $40 < r < 50\ m$. They refer to $> 5\ MeV$ shower electrons at a depth of 800 g/cm^2 generated by $10^2\ TeV$ photons. The distributions have been arbitrarily normalized so their peaks are the same for easier comparison by eye. The transverse angle distributions are symmetric around zero and wider at large distances. On the contrary the radial angle distributions are not symmetric but have a long tail increasing outward as the distance from the axis increases. In addition, the maxima of the radial distributions are shifted to larger positive angles.

As a result, the mean value of θ_R increases with increasing distance from the axis. The dependence of $< \theta_R >$ on r is shown in Fig. 23 at different depths in atmosphere.

A rather small dependence of $< \theta_R >$ on the atmospheric depth for particles close to the shower axis, $r \leq 30\ m$, can be noticed. At greater distances the decreasing of θ_R with depth could be ascribed to a geometric effect.

The mean value $< \theta_R >$ and the standard deviation σ_R at 800 g/cm^2 for three energies (10, 10^2, $10^3\ TeV$) are compared in Fig. 24. The radial dependence of both $< \theta_R >$ and σ_R is almost independent of energy, although the average angle increases slightly with increasing energy ($\sim 10\%$ per decade of energy).

As a result of this investigation we note that the mean angle $< \theta_R >$ varies linearly with the distance from the core ($\sim 3\ mrad/m$ up to 25 m), so that a good accuracy in determining the shower direction could be obtained only by fitting the entire angular distribution at small core distances. Accordingly, the uncertainty in the core location should be reduced at less than a few meters and the angles of electrons near the shower axis ($< 20\ m$) measured with sufficient accuracy (typically $< 1^0$). However, near the shower core high electron densities are expected, so that the possibility of an unbiased measurement of the angles of a large number of tracks should be properly investigated.

Results from further MonteCarlo runs show that the radial distribution of shower tracks exhibits a remarkable dependence on the energy threshold of the electrons at the detection level. Simulations have been performed for $10^2\ TeV$ primary photons at $800 g/cm^2$. In Fig. 25 the radial dependence of $< \theta_R >$ for different energy thresholds is shown. Results from these runs are summarized in Fig. 26 showing the dependence of $< \theta_R >$ on the threshold energy for a radial interval of $5 \div 15\ m$. Thus, one reaches the conclusion that the effective energy threshold for electron detection should be properly taken into account in comparing the experimental results to the MonteCarlo simulations. Moreover, we notice that shower photons, more abundant than electrons of a factor $5 \div 10$ depending on primary energy, threshold energy and depth, exhibit a narrower radial angular distribution (see fig. 26). Thus electrons from pair conversion could modify the radial distribution of shower tracks.

4. CONCLUSIONS

A fully three-dimensional MonteCarlo program (EPAS) has been developed in order to perform a detailed simulation of the atmospheric cascades initiated by high energy gamma rays. It has been used to carry out a series of simulations of air showers for primary gamma ray energy ranging from 0.1 to 10^3 TeV. Results concerning longitudinal, lateral, temporal and angular distributions of the electron component at different stages of the shower development are presented. Longitudinal development fluctuations of showers in the age range $0.9 \leq s_1 \leq 1.6$ have been parametrized by using a log-normal distribution. A direct comparison with other fully three-dimensional MonteCarlo simulations [22, 26] is only possible for the average longitudinal and lateral developments of showers in the low energy range $0.1 \div 10$ TeV: we find an excellent agreement and we extend the modifications to the usual Greisen parametrizations up to 10^3 TeV. Results concerning the photon component will be given in a separate paper.

The present version of the EPAS code will be implemented to include the photohadron production (to calculate the muon yield in γ-ray initiated showers) and the generation of the Cerenkov radiation. Once folded to the HEMAS simulation [6] of the atmospheric cascade initiated by hadron primaries the present code will provide detailed information about the electromagnetic component of the extensive air showers.

ACKNOWLEDGMENTS

The authors are grateful to T.K. Gaisser for his comments and suggestions.

References

[1] B. Rossi, High-Energy Particles (Englewood Cliffs, N.J.: Prentice-Hall 1952).

[2] I.Y.Crewther and R.J.Protheroe, J. Phys. G: Nucl. Phys. 16 (1990) L13.

[3] S. Mikocki at al., J.Phys.G: Nucl. Phys. 17 (1991) 1303.

[4] A.M. Hillas, in: Proc. of the 17th Int. Cosmic Ray Conf. (Paris, 1981) 8 p.193.

[5] K. Kasahara, Computer Physics Communications 64 (1991) 235.

[6] C. Forti et al., Phys. Rev. D 42 (1990) 3668.

[7] M. Aglietta et al., Nucl. Instr. and Meth. A 277 (1989) 23.

[8] I.B. Bernstein, Phys. Rev. 80 (1950) 995.

[9] H.A. Bethe and J. Askhin, in: Experimental Nuclear Physics ed. E. Segre (Wiley, 1953) vol. 1 252.

[10] O. Klein and Y. Nishina, Z. fur Physik 52 (1929) 853.

[11] I. Pratt, Phys. Rev. 120 (1961) 1717.

[12] C. Moller, Ann. Physik 14 (1932) 531
H.J. Bhabha, Proc. Roy. Soc. A 154 (London, 1936) 195.

[13] R.M. Sternheimer et al., Phys. Rev. B 26 (1982) 6067.

[14] W. Heitler, in: The Quantum Theory of Radiation (Clarendon Press, Oxford 1954).

[15] H.A. Bethe, Phys. Rev. 89 (1953) 1256.

[16] V.L. Highland, Nucl. Instr. and Meth. A 129 (1975) 497.

[17] J. Nishimura, Handbuck der Physik (Springer-Verlag, 1967) vol. 2 p. 1.

[18] G.R. Lynch and O.I. Dahl, Nucl. Instr. and Meth. B 58 (1991) 6.

[19] C.N. Yang, Phys. Rev. Lett. 84 (1951) 599.

[20] H. Messel and D.F. Crawford, Electron-Photon Shower Distribution Function (Pergamon Press, 1970).

[21] K. Greisen, in: Progress in Cosmic Ray Physics, (1956) vol. 3 p. 3.

[22] E.J. Fenyves et al., Phys. Rev. D 37 (1988) 649.

[23] A.M. Hillas, J. Phys. G: Nucl. Phys. 8 (1982) 1461.

[24] J.A. Richards and L.W. Nordheim, Phys. Rev. 74 (1948) 1106.

[25] J.N. Capdevielle et al., J. Phys. G: Nucl. Phys. 8 (1982) 1317.

[26] A.M. Hillas and J. Lapikens, in: Proc. of the 15th Int. Cosmic Ray Conf. (Plovdiv, 1977) vol. 6 p. 460.

[27] I.Y. Crewther and R.J. Protheroe, J. Phys. G: Nucl. Phys. 18 (1992) 205.

[28] B. D'Ettorre Piazzoli and G. Di Sciascio, in: Proc. of the 22th Int. Cosmic Ray Conf. (Dublin, 1991) vol. 4 p. 516.

[29] J. Poirier et al., Phys. Rev. D 36 (1987) 1378.

TABLE I

$E_{th}(MeV)$	$A_e(E_{th})$	$a_e(E_{th})$
5	0.75	0.19
10	0.63	0.35
15	0.54	0.45
20	0.50	0.53
50	0.32	0.83
100	0.21	1.20
500	$5.6 \cdot 10^{-2}$	2.18
10^3	$2.4 \cdot 10^{-2}$	2.74

Figure Captions

1. Distribution of the fractional electron energy $v(= E_e/E_\gamma)$ for pair production at three energies. Solid lines correspond to the theoretical prediction of Bernstein [8], crosses refer to the MonteCarlo sampling.

2. Ionization energy loss (solid line) according to the Bethe-Block formula. The dashed line represents the energy loss involving transfers less than 2 MeV.

3. Electron scattering distributions for different energies and step lengths: comparison between distributions obtained in the gaussian approximation using different mean scattering angles (cross: [1], diamond: [15], star: [16], circle: [17]) and the prediction of the Moliere theory (solid line).

4. Lateral distribution of the electron component of photon-initiated showers ($E_\gamma = 1\ TeV$, $s_1 = 1$) with $E_{th} = 5\ MeV$ electron threshold energy. Diamonds are obtained using the gaussian approximation with the Highland mean scattering angle [16], crossed points refer to the Moliere theory.

5. Longitudinal development of the electron component of photon-initiated showers with $E_{th} = 5\ MeV$ electron threshold energy (cross: MonteCarlo, solid line: formula (1)).

6. Same curves as in Fig. 5 with the dispersion σ_d around the average value superimposed.

7. $\sigma_d/\overline{N}_e$ versus depth in atmosphere for different primary photon energies.

8. Comparison between the Greisen value $\overline{N}_e$ and the mean size $\overline{N}_e(\mu_{10}, \sigma_{10})$ obtained from formula (8).

9. Size distribution at depth of 800 g/cm^2 for showers initiated by $10, 10^2, 10^3\ TeV$ photons (histogram: a), b), c) respectively). The solid lines is obtained using the parametrization given in the text. The horizontal scale has been divided by a factor 10^3.

10. The integral energy spectrum of electrons for different photon energies at various depths in atmosphere from 4 to 24 r.l.

11. The integral energy spectrum of electrons and photons at the shower maximum compared to the calculations made by Richards and Nordheim (solid lines) for three energies. The ordinate gives the number of particles with energy exceeding E, normalized to the total number of electron.

12. Lateral distribution of the electron component of showers generated by $0.1, 1, 10, 10^2 TeV$ photons at t= 4, 10, 16 r.l. above 850 g/cm^2 (cross: 4 r.l., diamond: 10 r.l., circle: 16 r.l.). The electron threshold energy is 5 MeV. The lines show the modified NKG formula (10) compared to results of the MonteCarlo simulation.

13. Lateral distribution of the electron component of photon-initiated shower with $E_{th} = 5\ MeV$ electron threshold energy at 800 g/cm^2. Comparison between MonteCarlo data, modified NKG formula (10) and original NKG formula.

14. Lateral distribution of electrons and photons for $10^3\ TeV$ showers at 800 g/cm^2. The threshold for photons is also $5\ MeV$.

15. Lateral distribution of electrons for $10^3\ TeV$ at 800 g/cm^2. Curves show NKG type fits with different values of r_M (for r_M= 10, 50, 100 m we find s_2= 1.76, 1.07, 0.81 respectively).

16. Time distribution of the electron component of $10^2\ TeV$ photon-initiated showers at 800 g/cm^2 as a function of the core distance. The electron threshold energy is 5 MeV.

17. Average particle delay and full width at half maximum of the electron component of $10^2\,TeV$ photon-initiated showers as a function of the core distance at different stages of the longitudinal development. The electron threshold energy is 5 MeV.

18. Average time delay of the electron component for different primary energies and for three values of s_1.

19. Distribution of the arrival time of the first particle, t_1 at different radial distances for showers generated by photons of $10^2\,TeV$ at $s_1 = 1.4$.

20. Average arrival time of the first particle as a function of the core distance for different photon energies at increasing s_1.

21. Integral time delay distributions of the first electron recorded by increasing size detectors at 50 m from shower axis for $10^2\,TeV$ a) and $10^3\,TeV$ b) showers at 800 g/cm^2. The time distribution of the first electron hitting into the radial interval $45 \div 55\,m$ is shown for comparison.

22. Radial (a) and transverse (b) distributions of secondary electrons of showers generated by $10^2\,TeV$ photons for radial distances (0-10) m (dashed histogram) and (40-50) m (solid histogram) at 800 g/cm^2.

23. Dependence of $< \theta_R >$ on the core distance at different depths in atmosphere for showers initiated by $10^2\,TeV$ photons.

24. Dependence of $< \theta_R >$ and σ_R on the core distance at 800 g/cm^2 for showers initiated by 10, 10^2, $10^3\,TeV$ photons.

25. Dependence of $< \theta_R >$ on the core distance for different energy thresholds of secondary electrons in showers initiated by $10^2\,TeV$ photons at 800 g/cm^2.

26. Dependence of $< \theta_R >$ on the threshold energy E for secondary electrons and photons ($5 < r < 15\,m$) in showers initiated by $10^2\,TeV$ photons at 800 g/cm^2 .

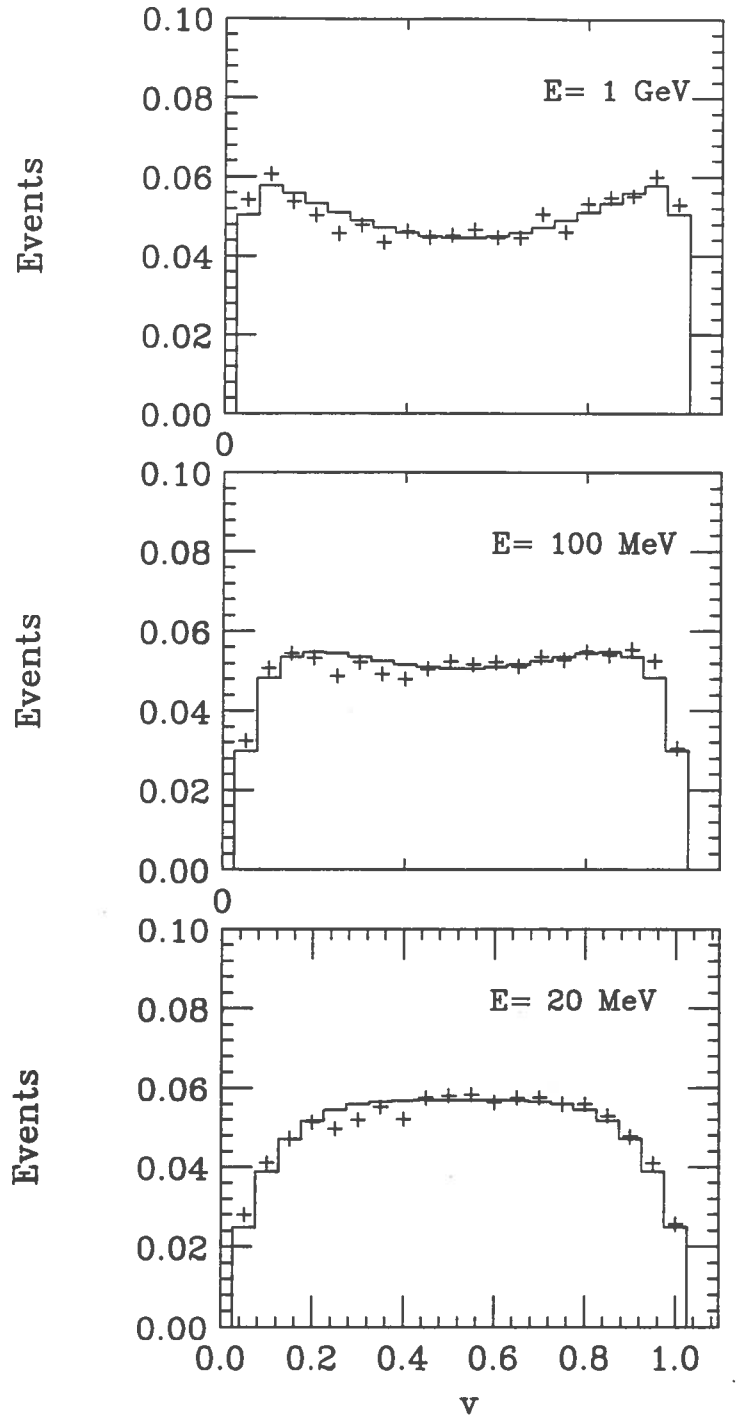
E= 1 GeV
E= 100 MeV
E= 20 MeV
Events
Events
Events
0.10
0.08
0.06
0.04
0.02
0.00
0
0.0
0.2
0.4
0.6
0.8
1.0
v

FIG. 1

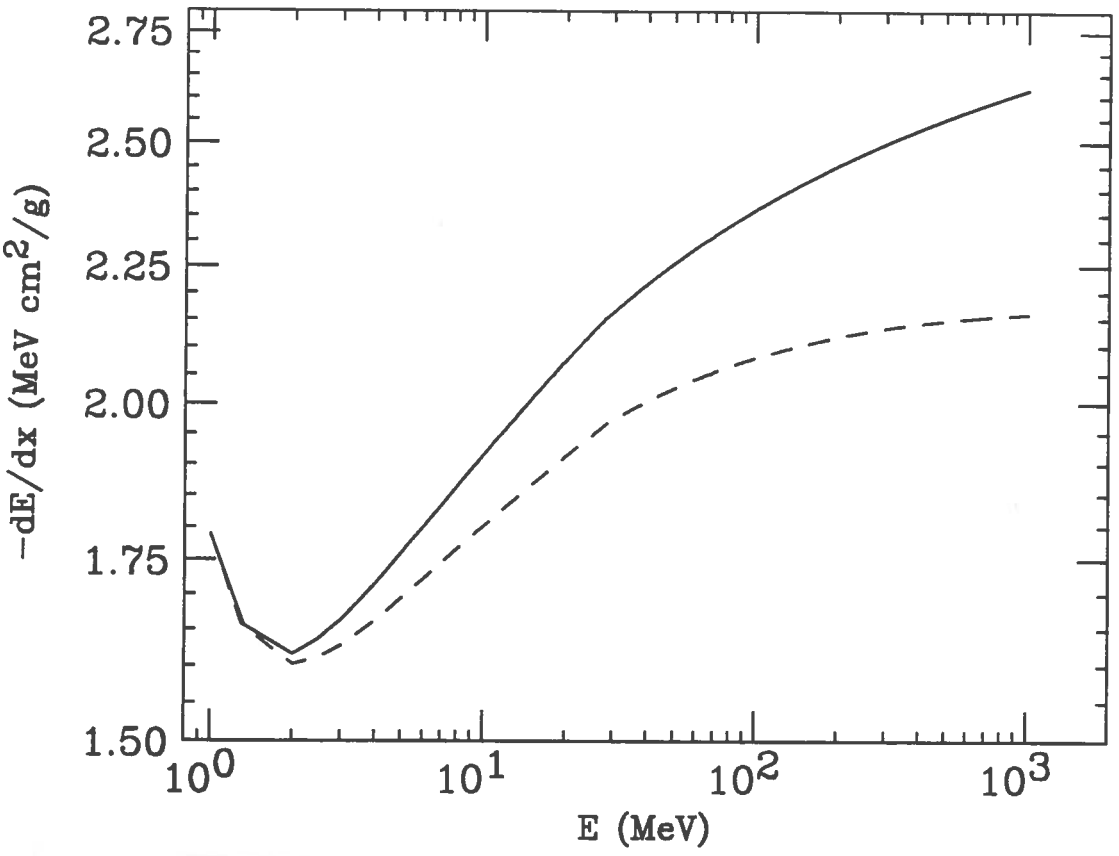

FIG. 2

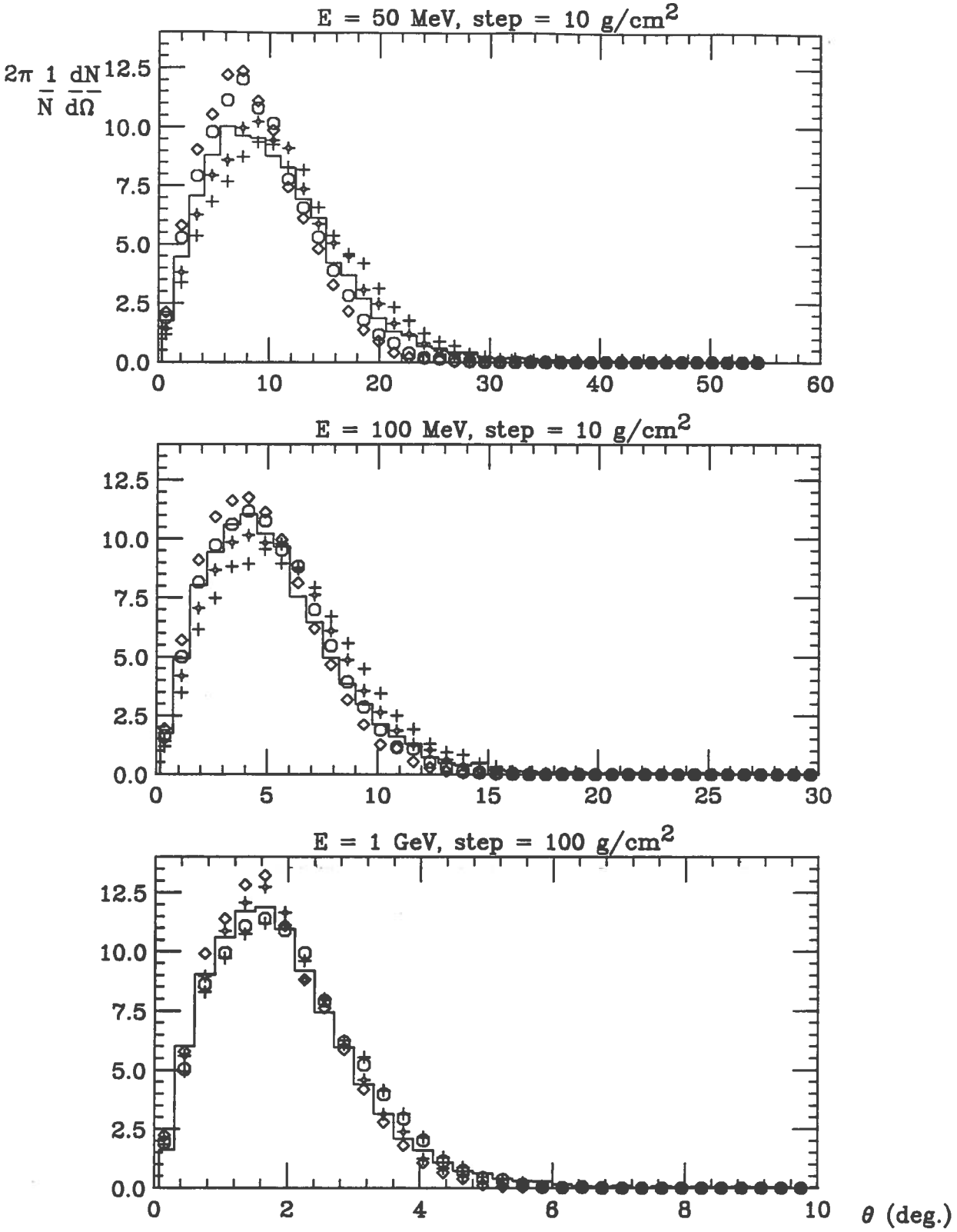
E = 50 MeV, step = 10 g/cm2
E = 100 MeV, step = 10 g/cm2
E = 1 GeV, step = 100 g/cm2
2π 1 dN / N dΩ
θ (deg.)

FIG. 3

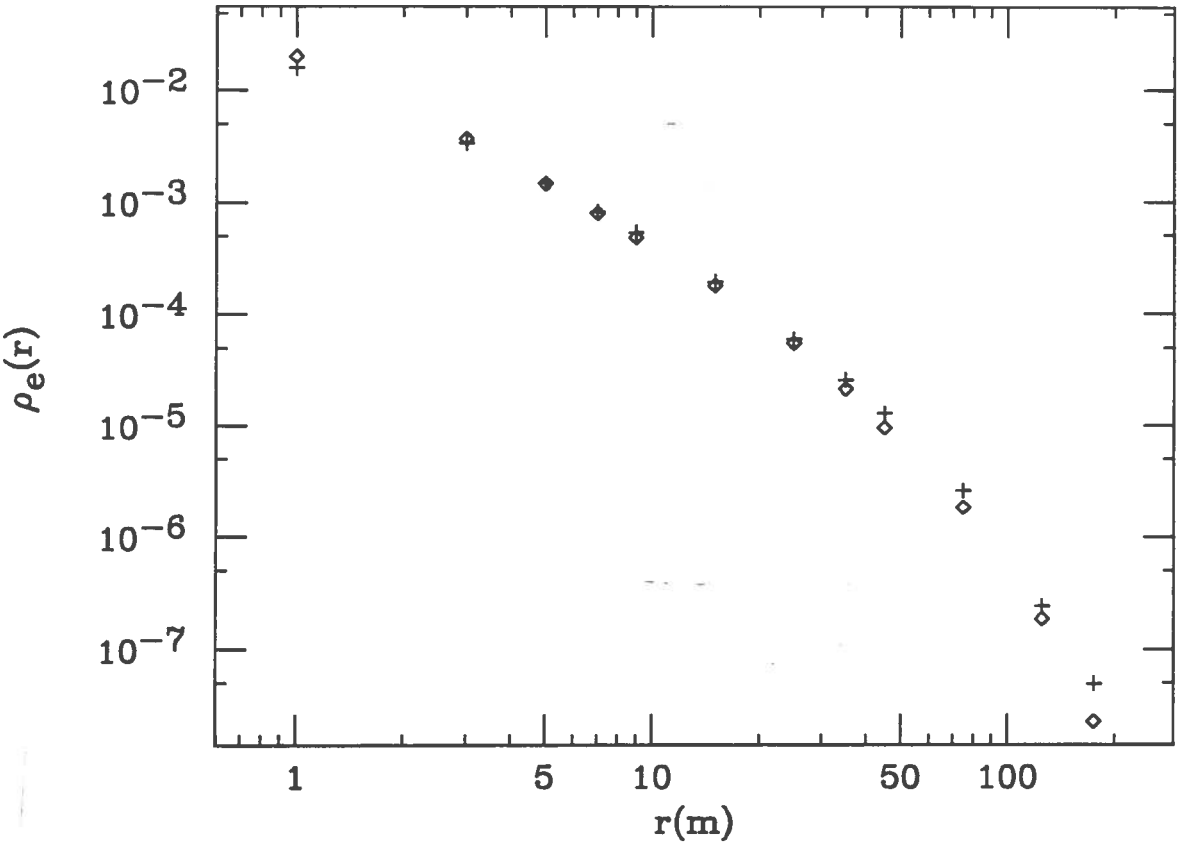

FIG. 4

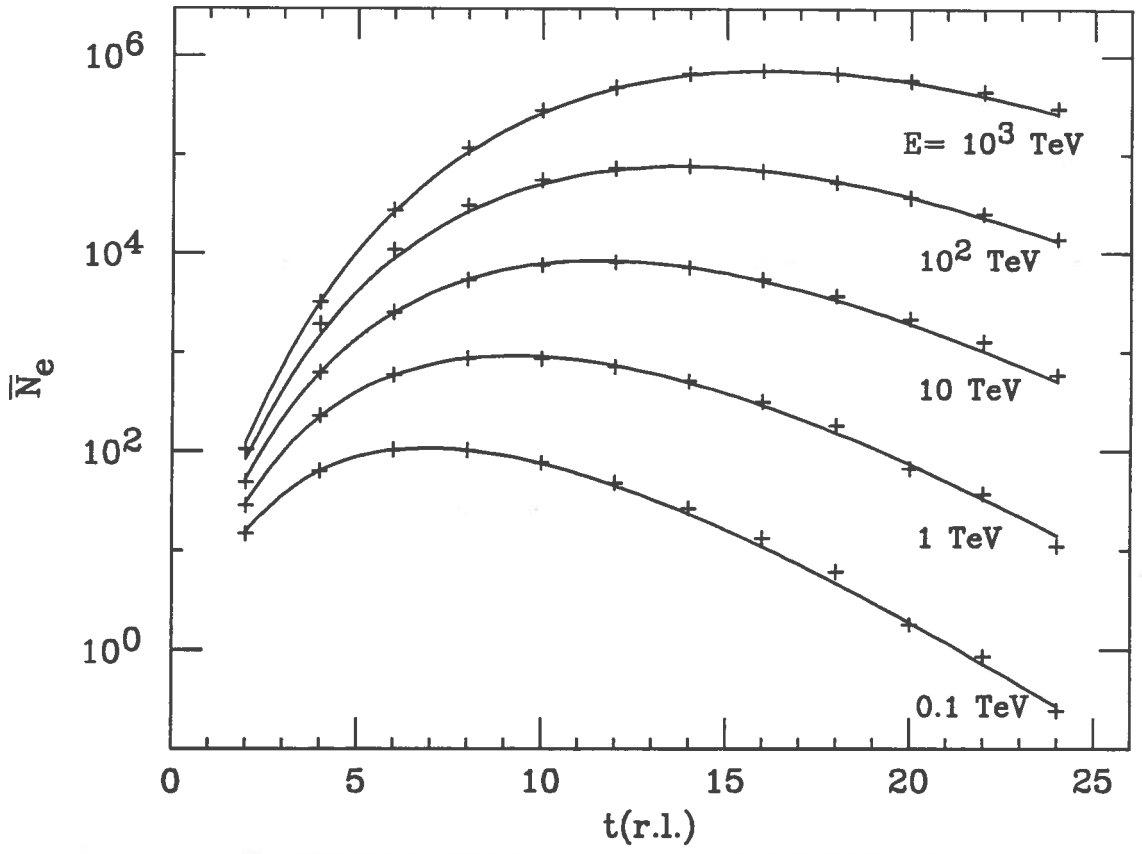
10^6
10^4
10^2
10^0
$\bar{N}_e$
E= 10^3 TeV
10^2 TeV
10 TeV
1 TeV
0.1 TeV
0
5
10
15
20
25
t(r.l.)

FIG. 5

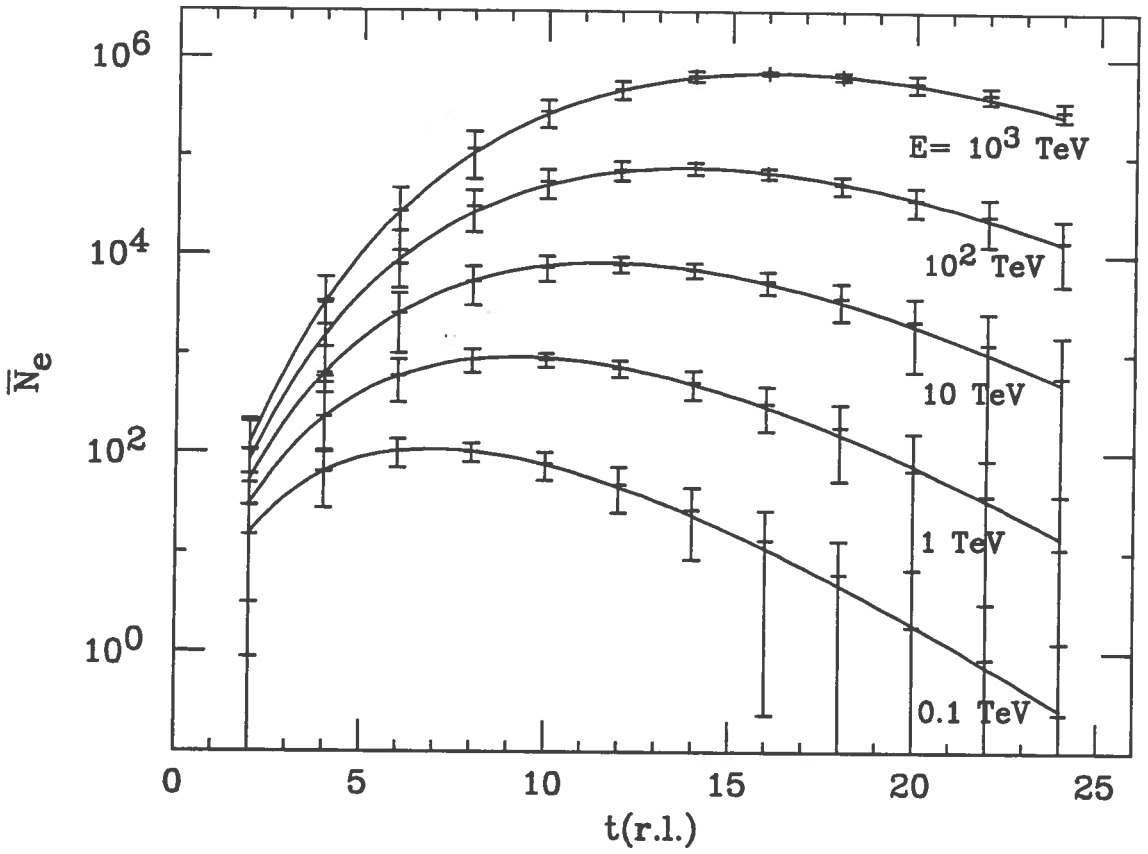
10^6
10^4
10^2
10^0
$\bar{N}_e$
E= 10^3 TeV
10^2 TeV
10 TeV
1 TeV
0.1 TeV
0
5
10
15
20
25
t(r.l.)

FIG. 6

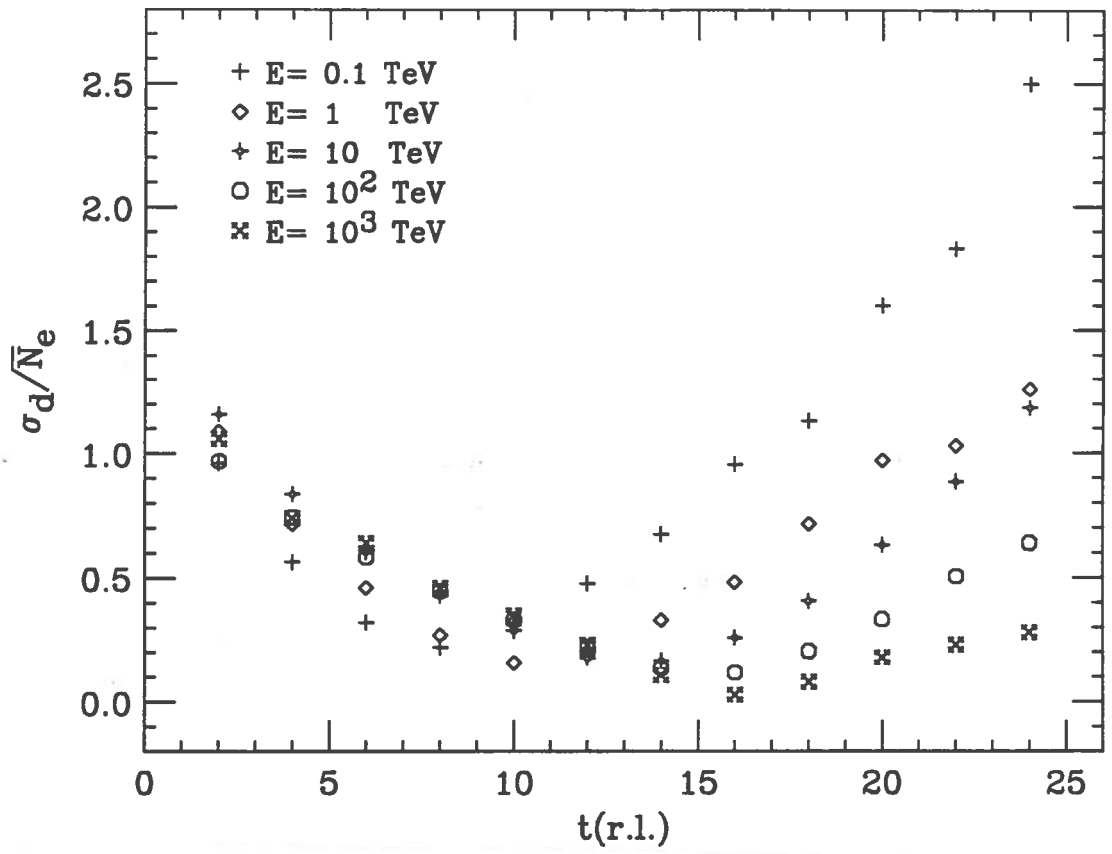
+ E= 0.1 TeV
◇ E= 1 TeV
+ E= 10 TeV
○ E= 10^2 TeV
× E= 10^3 TeV
σd/N̄e
t(r.l.)
0.0
0.5
1.0
1.5
2.0
2.5
0
5
10
15
20
25

FIG. 7

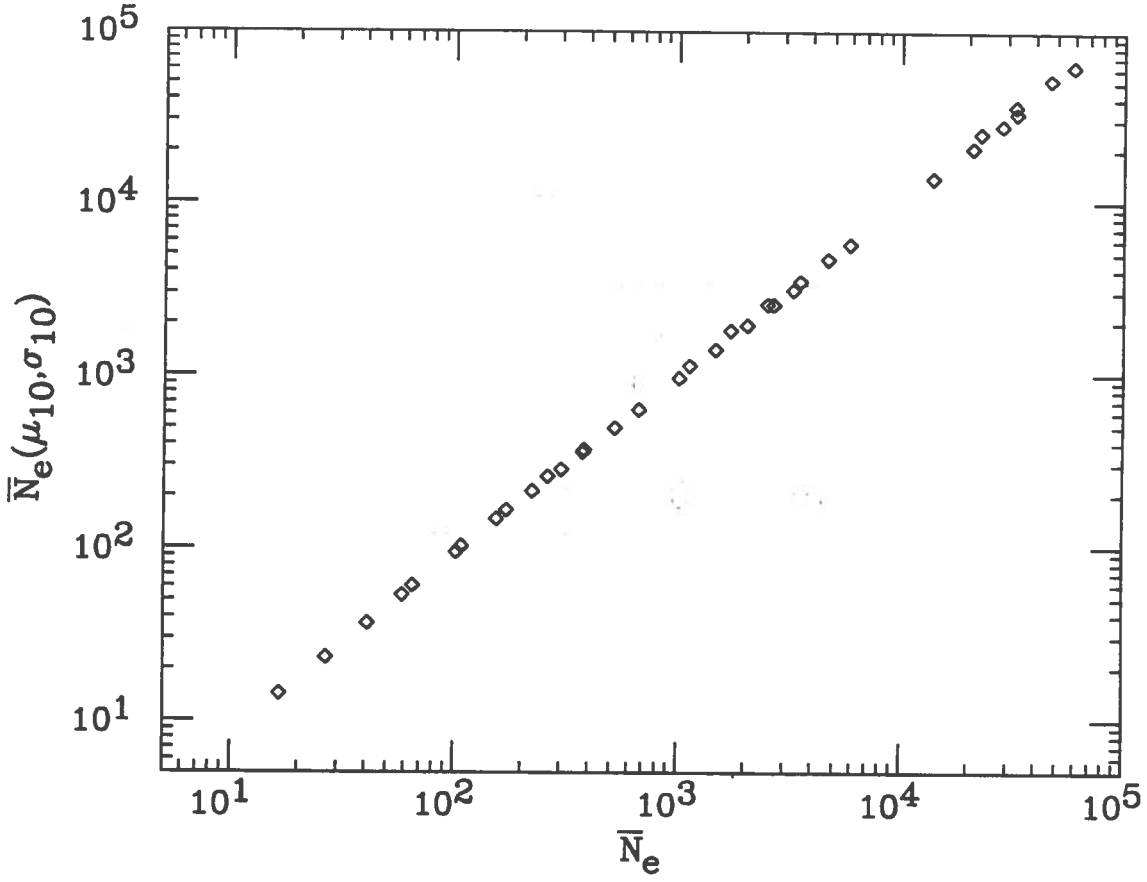
10^5
10^4
10^3
10^2
10^1
$\bar{N}_e(\mu_{10},\sigma_{10})$
10^1
10^2
10^3
10^4
10^5
$\bar{N}_e$

FIG. 8

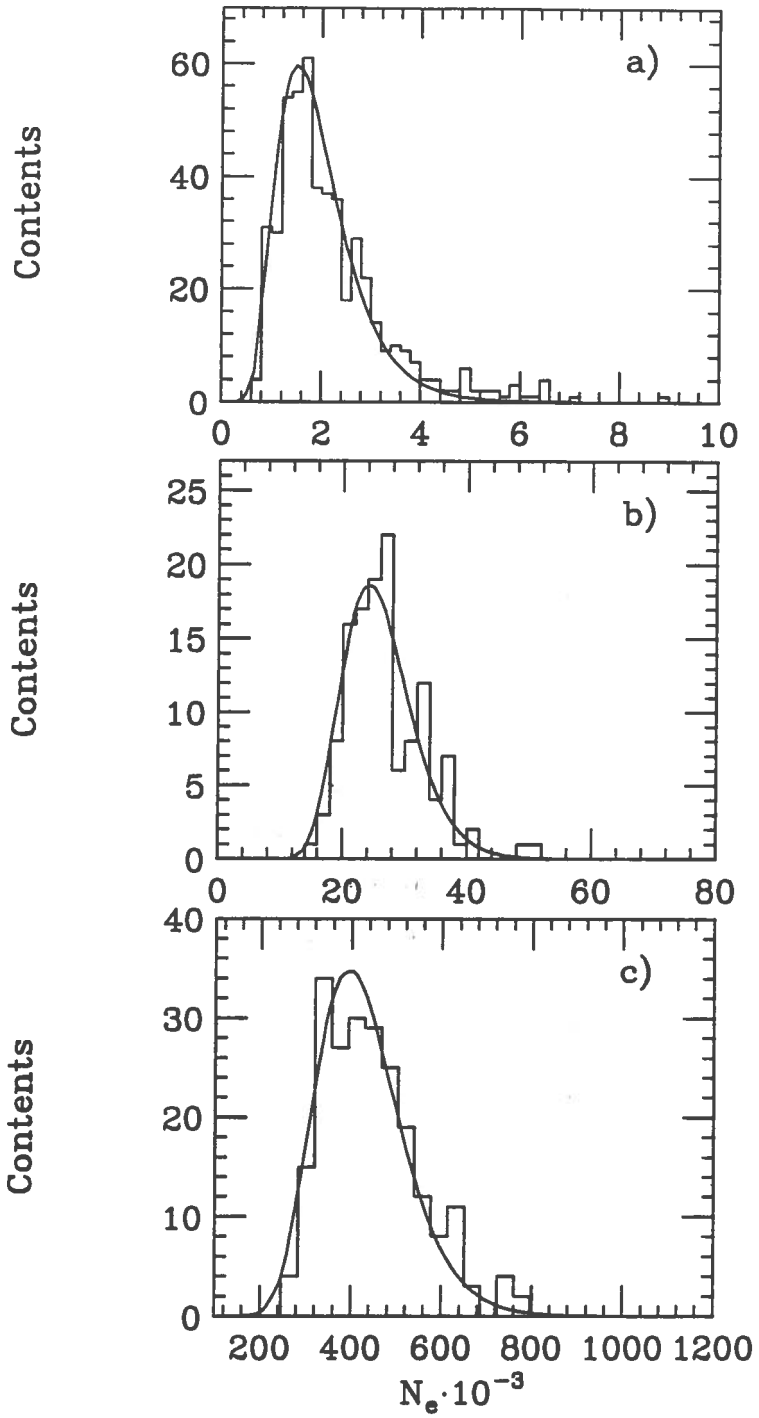

FIG. 9

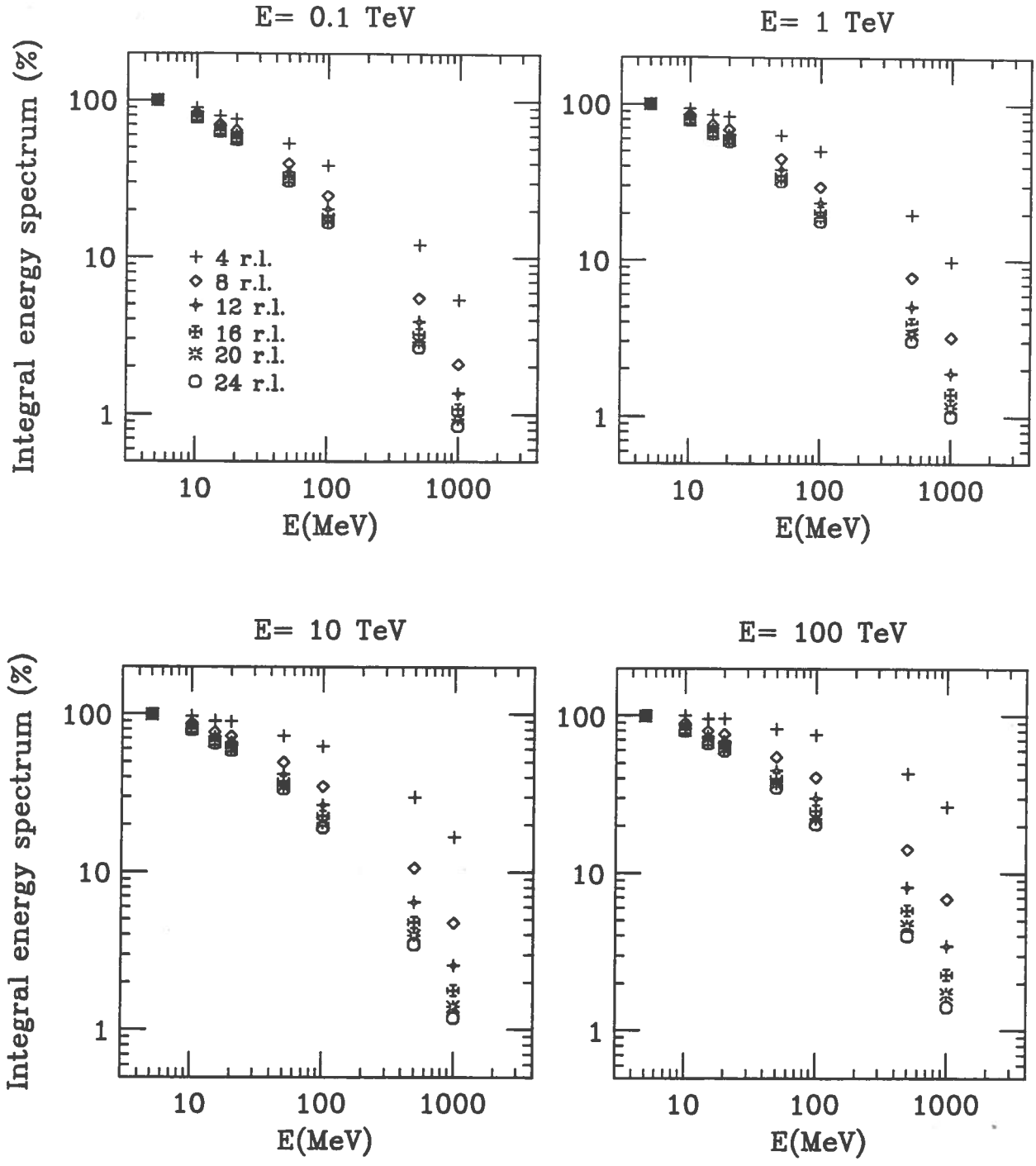
E= 0.1 TeV
E= 1 TeV
E= 10 TeV
E= 100 TeV
Integral energy spectrum (%)
E(MeV)
100
10
1
10
100
1000
4 r.l.
8 r.l.
12 r.l.
16 r.l.
20 r.l.
24 r.l.

FIG. 10

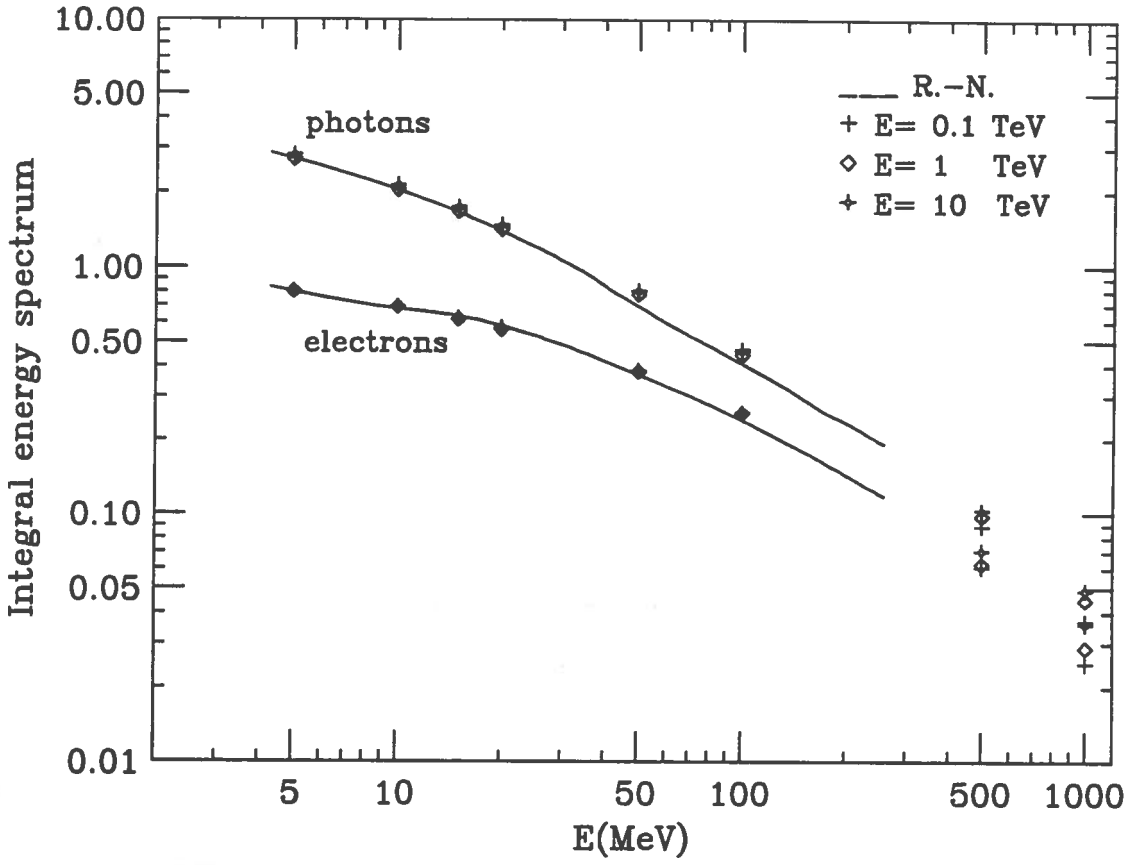
10.00
5.00
1.00
0.50
0.10
0.05
0.01
Integral energy spectrum
photons
electrons
R.–N.
E= 0.1 TeV
E= 1 TeV
E= 10 TeV
5
10
50
100
500
1000
E(MeV)

FIG. 11

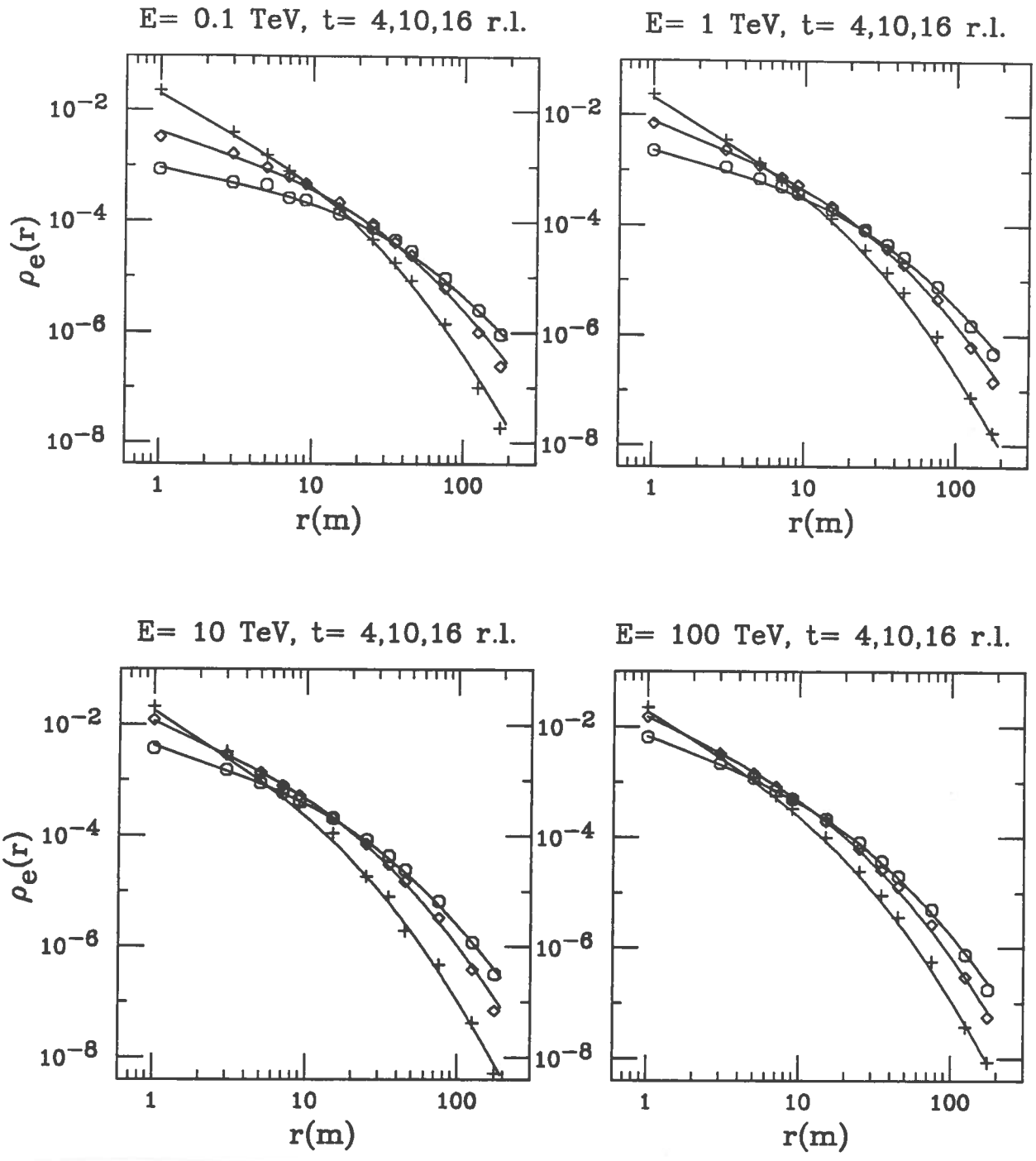
E= 0.1 TeV, t= 4,10,16 r.l.
E= 1 TeV, t= 4,10,16 r.l.
E= 10 TeV, t= 4,10,16 r.l.
E= 100 TeV, t= 4,10,16 r.l.
$\rho_e(r)$
10^{-2}
10^{-4}
10^{-6}
10^{-8}
1
10
100
r(m)

FIG.12

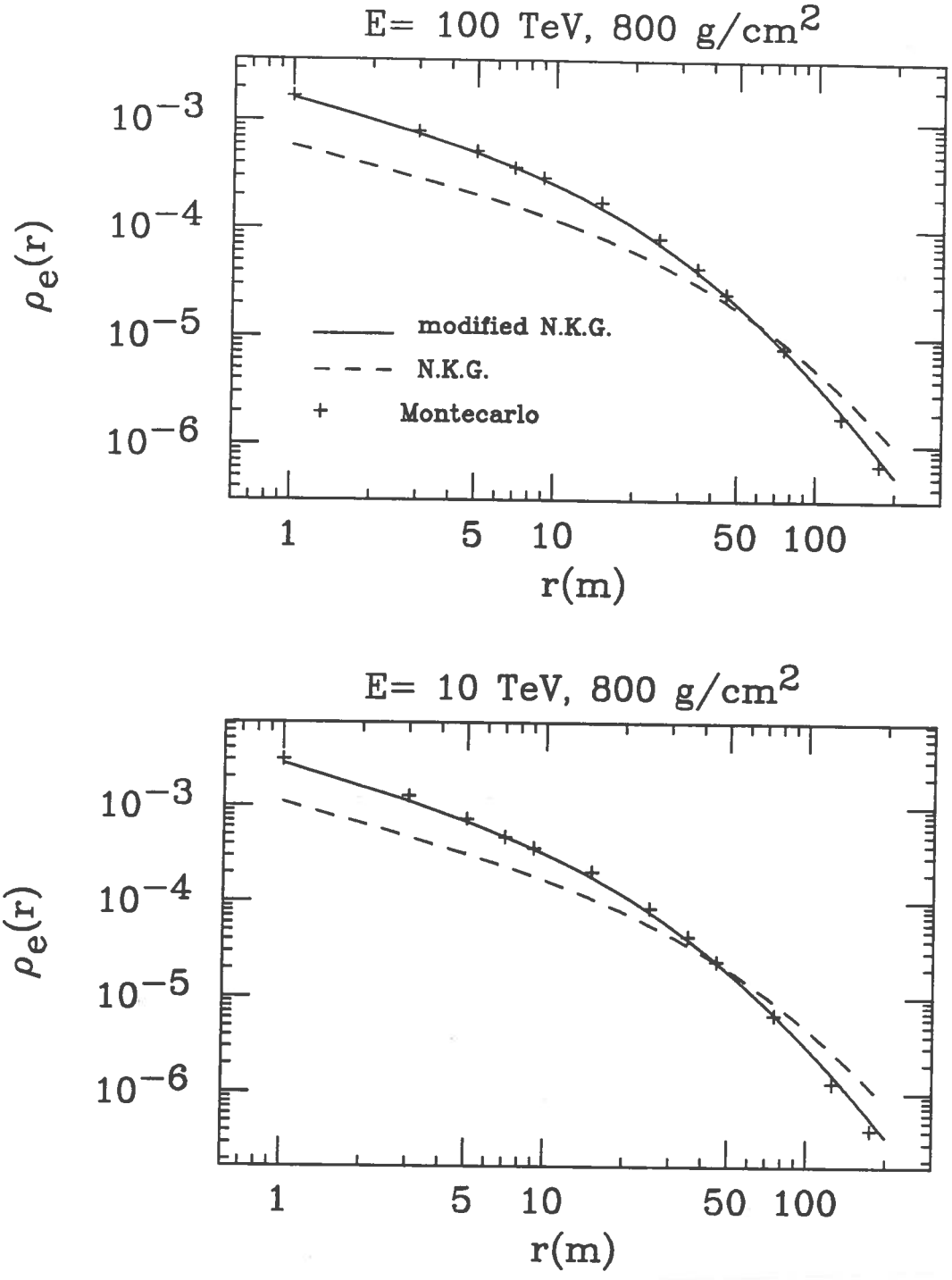
E= 100 TeV, 800 g/cm2
$\rho_e(r)$
10^{-3}
10^{-4}
10^{-5}
10^{-6}
modified N.K.G.
N.K.G.
Montecarlo
1
5
10
50
100
r(m)
E= 10 TeV, 800 g/cm2
$\rho_e(r)$
10^{-3}
10^{-4}
10^{-5}
10^{-6}
1
5
10
50
100
r(m)

FIG.13

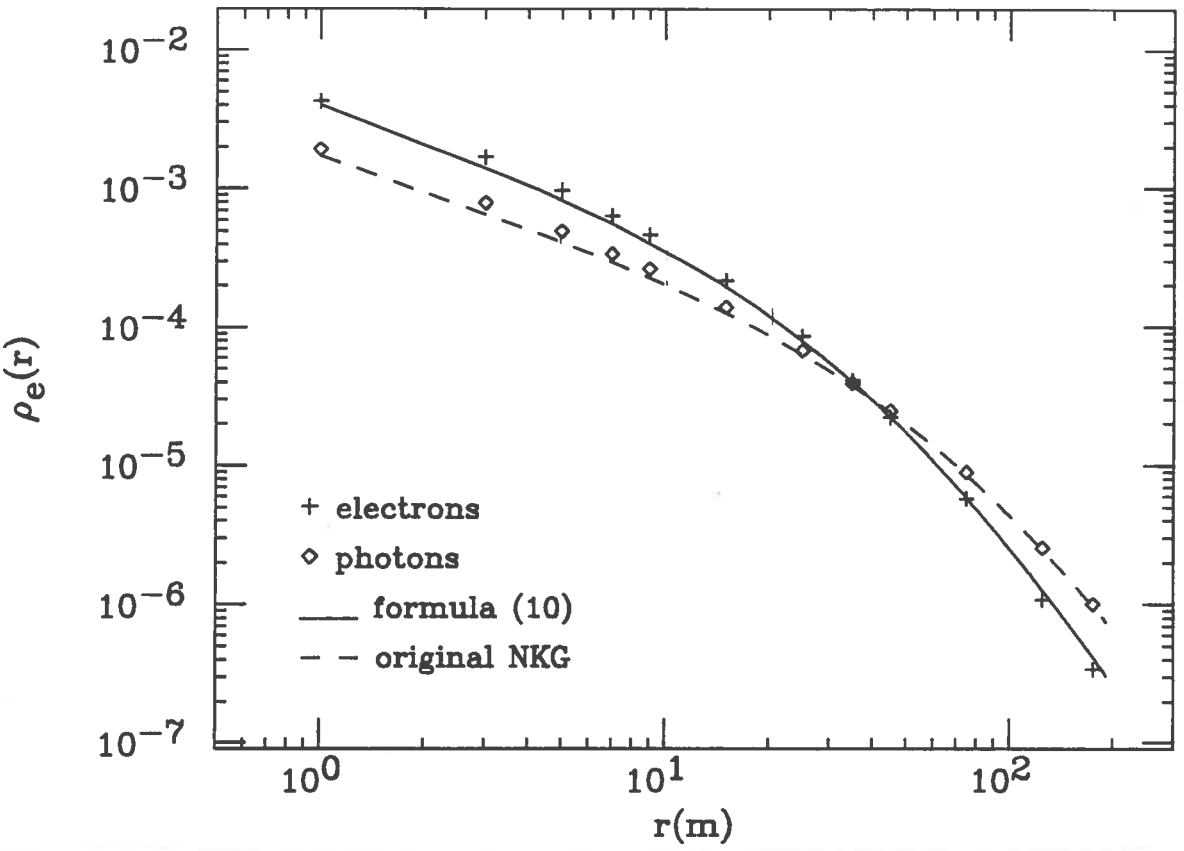
10^{-2}
10^{-3}
10^{-4}
10^{-5}
10^{-6}
10^{-7}
$\rho_e(r)$
+ electrons
◇ photons
____ formula (10)
– – original NKG
10^0
10^1
10^2
r(m)

FIG. 14

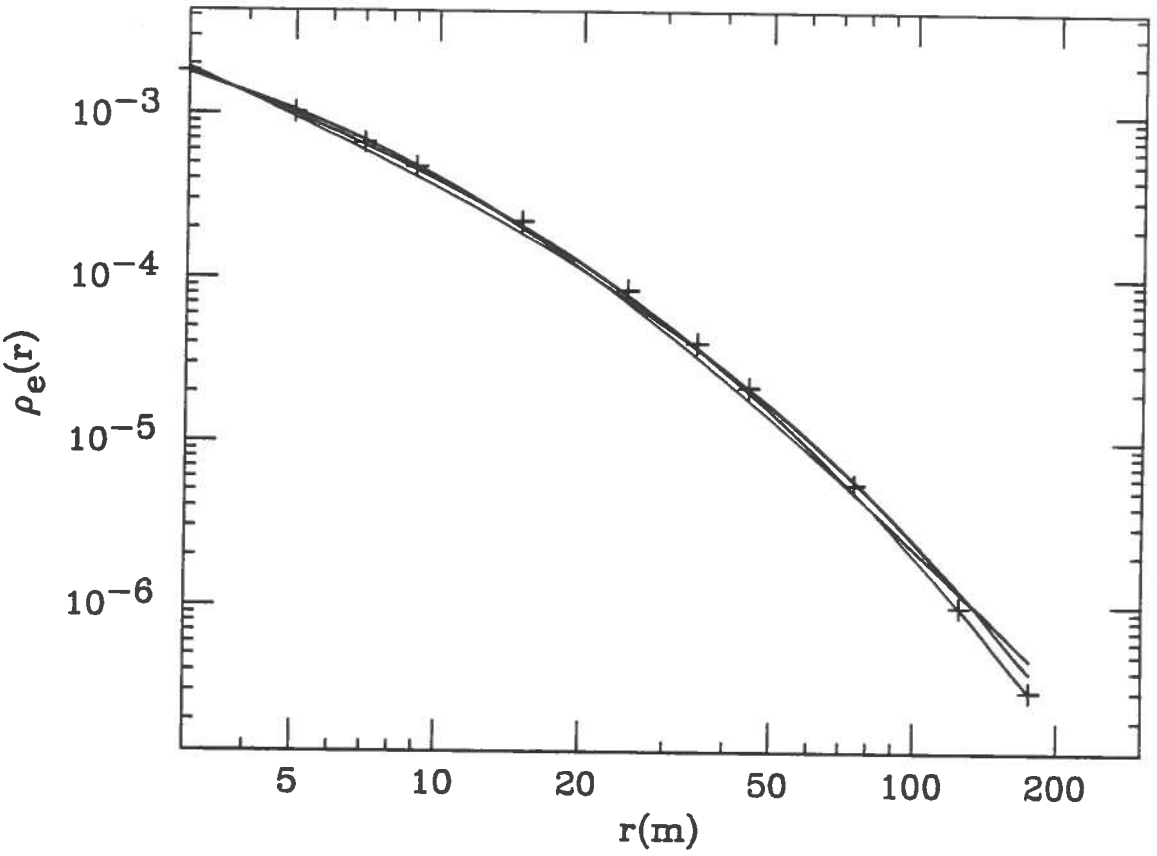

FIG. 15

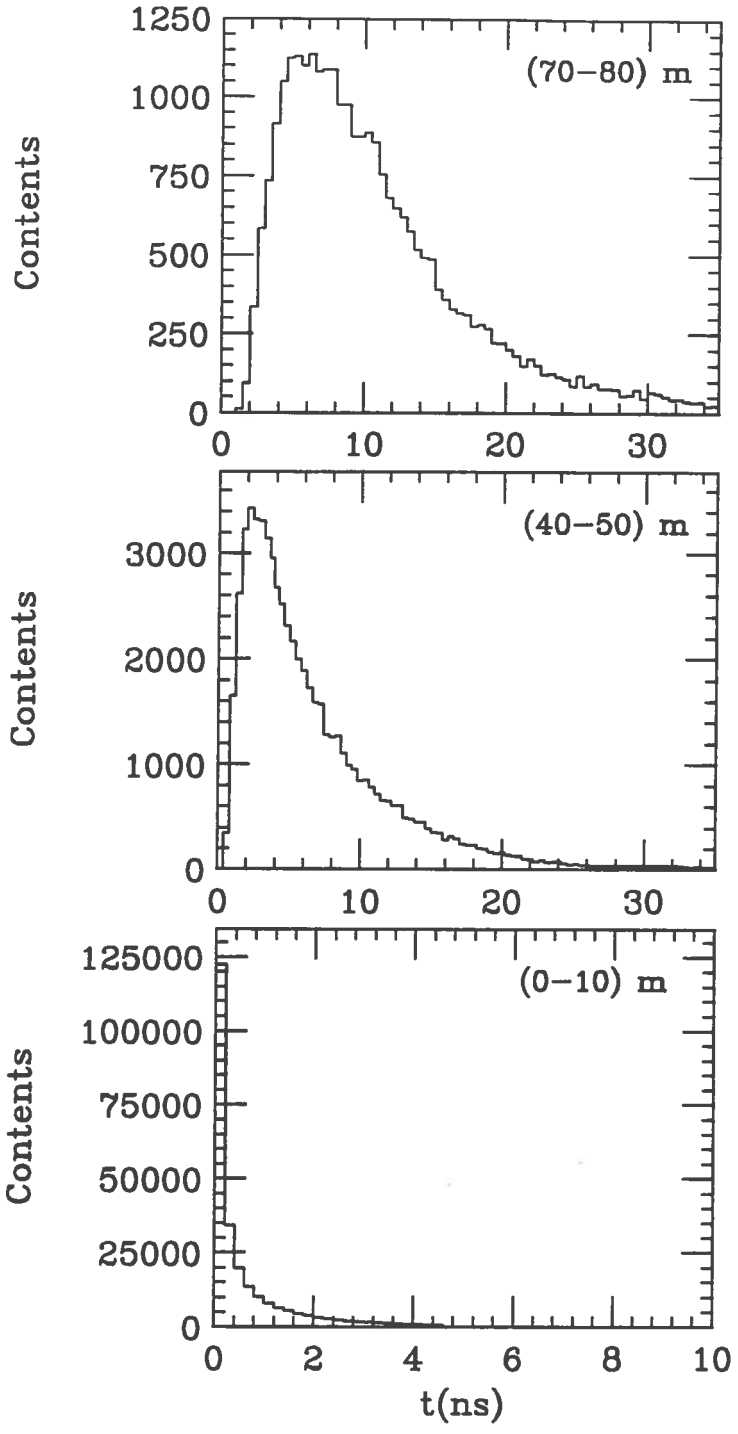

FIG. 16

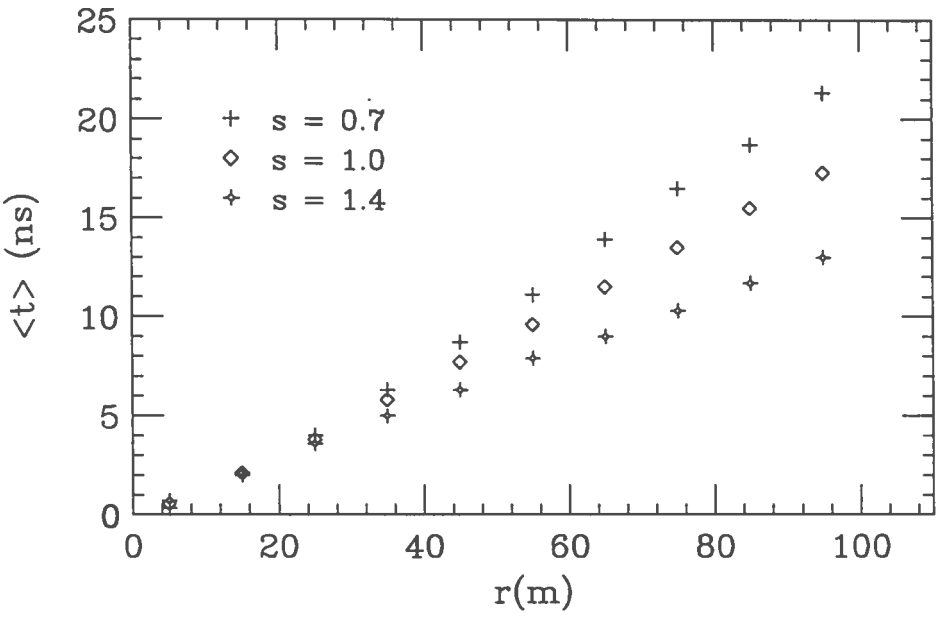
25
20
15
10
5
0
<t> (ns)
s = 0.7
s = 1.0
s = 1.4
0
20
40
60
80
100
r(m)

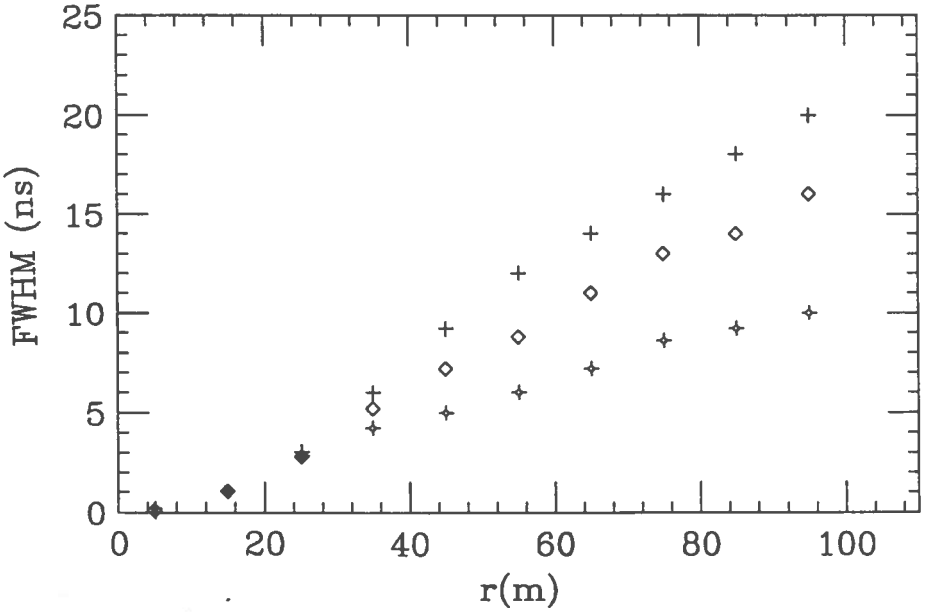
25
20
15
10
5
0
FWHM (ns)
0
20
40
60
80
100
r(m)

FIG. 17

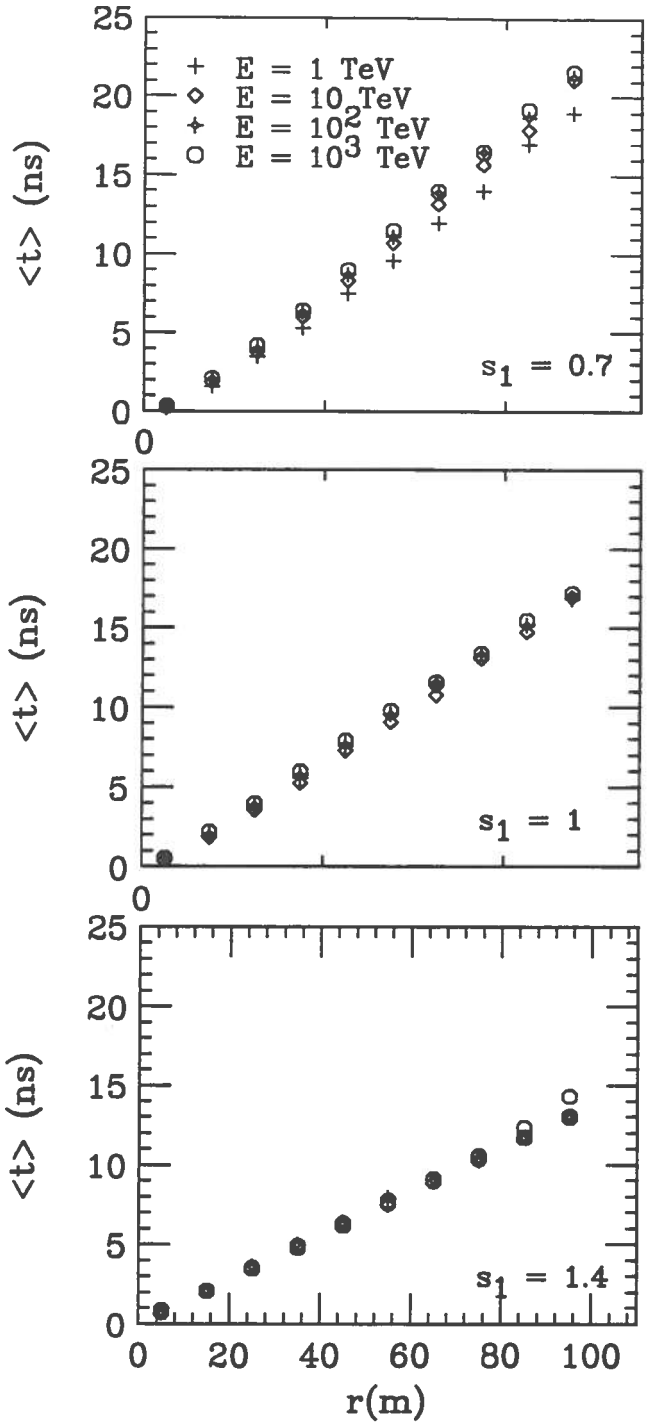
E = 1 TeV
E = 10 TeV
E = 10^2 TeV
E = 10^3 TeV
s1 = 0.7
s1 = 1
s1 = 1.4
<t> (ns)
r(m)
0
5
10
15
20
25
0
20
40
60
80
100

FIG. 18

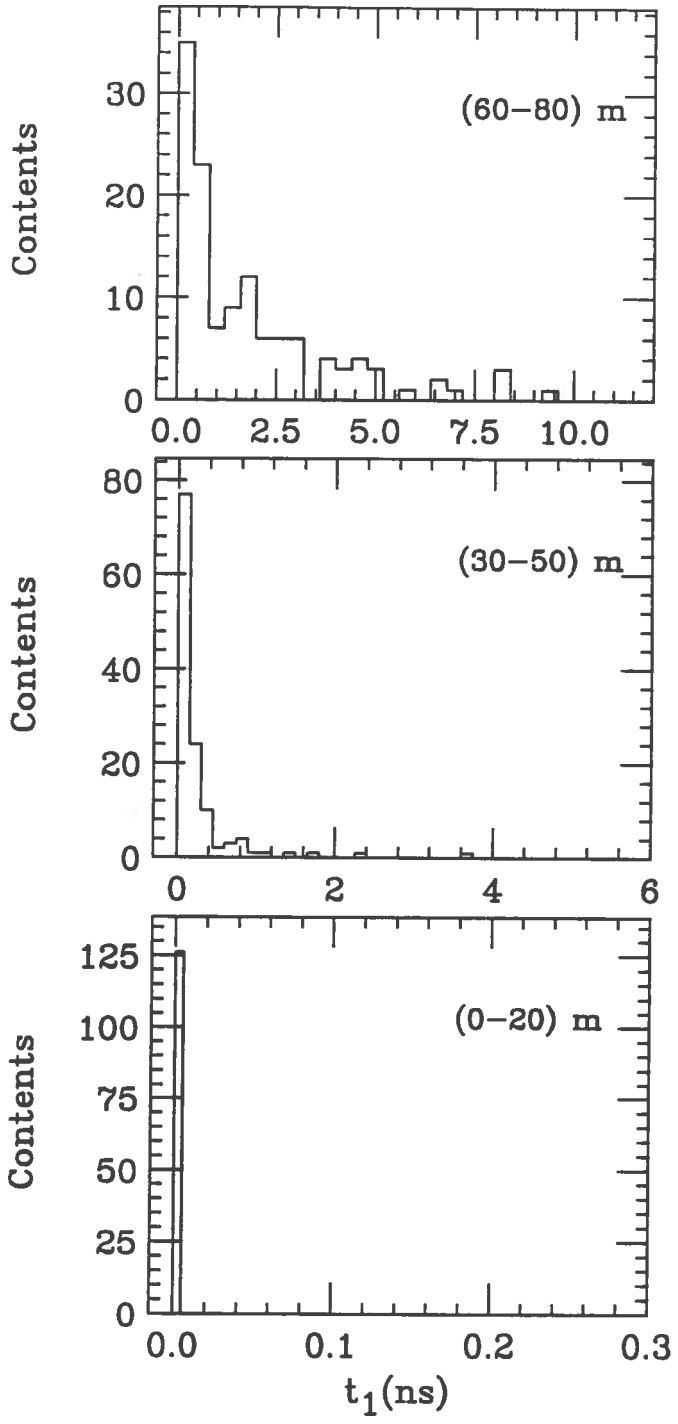
Contents
30
20
10
0
0.0
2.5
5.0
7.5
10.0
(60–80) m
Contents
80
60
40
20
0
0
2
4
6
(30–50) m
Contents
125
100
75
50
25
0
0.0
0.1
0.2
0.3
(0–20) m
t_1(ns)

FIG. 19

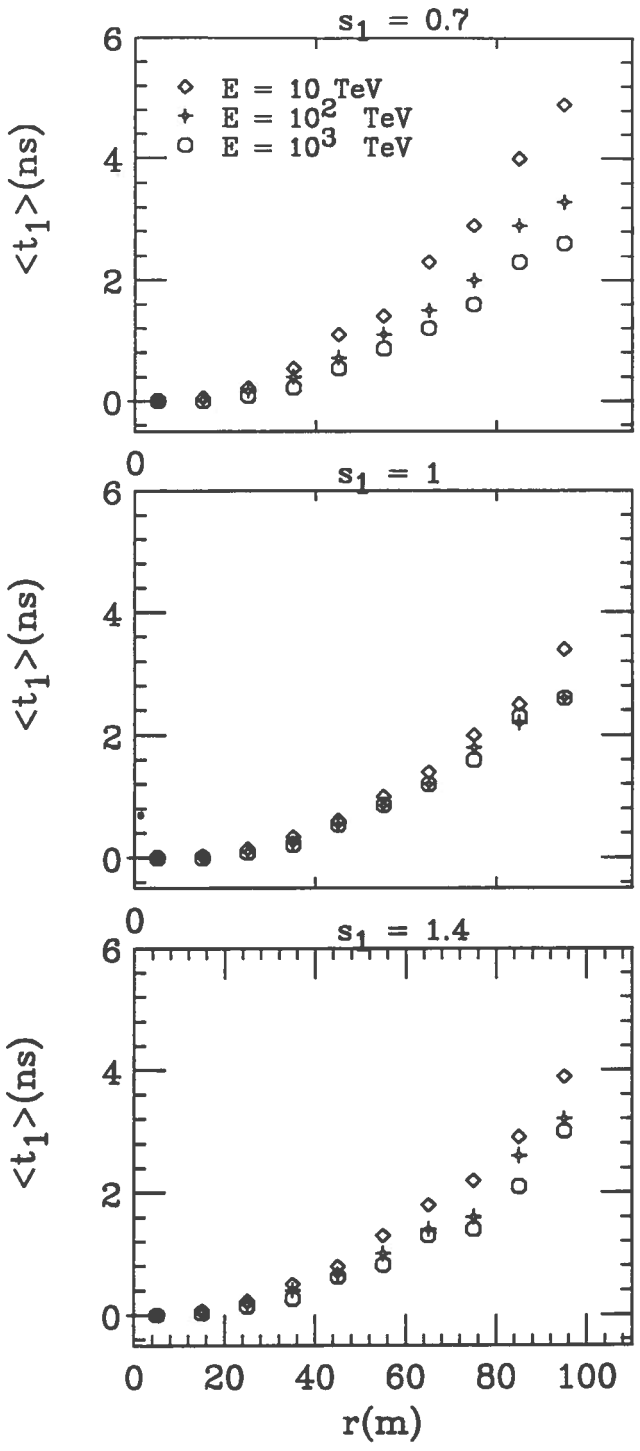
s_1 = 0.7
E = 10 TeV
E = 10^2 TeV
E = 10^3 TeV
s_1 = 1
s_1 = 1.4
<t_1>(ns)
r(m)
0
2
4
6
0
20
40
60
80
100

FIG. 20

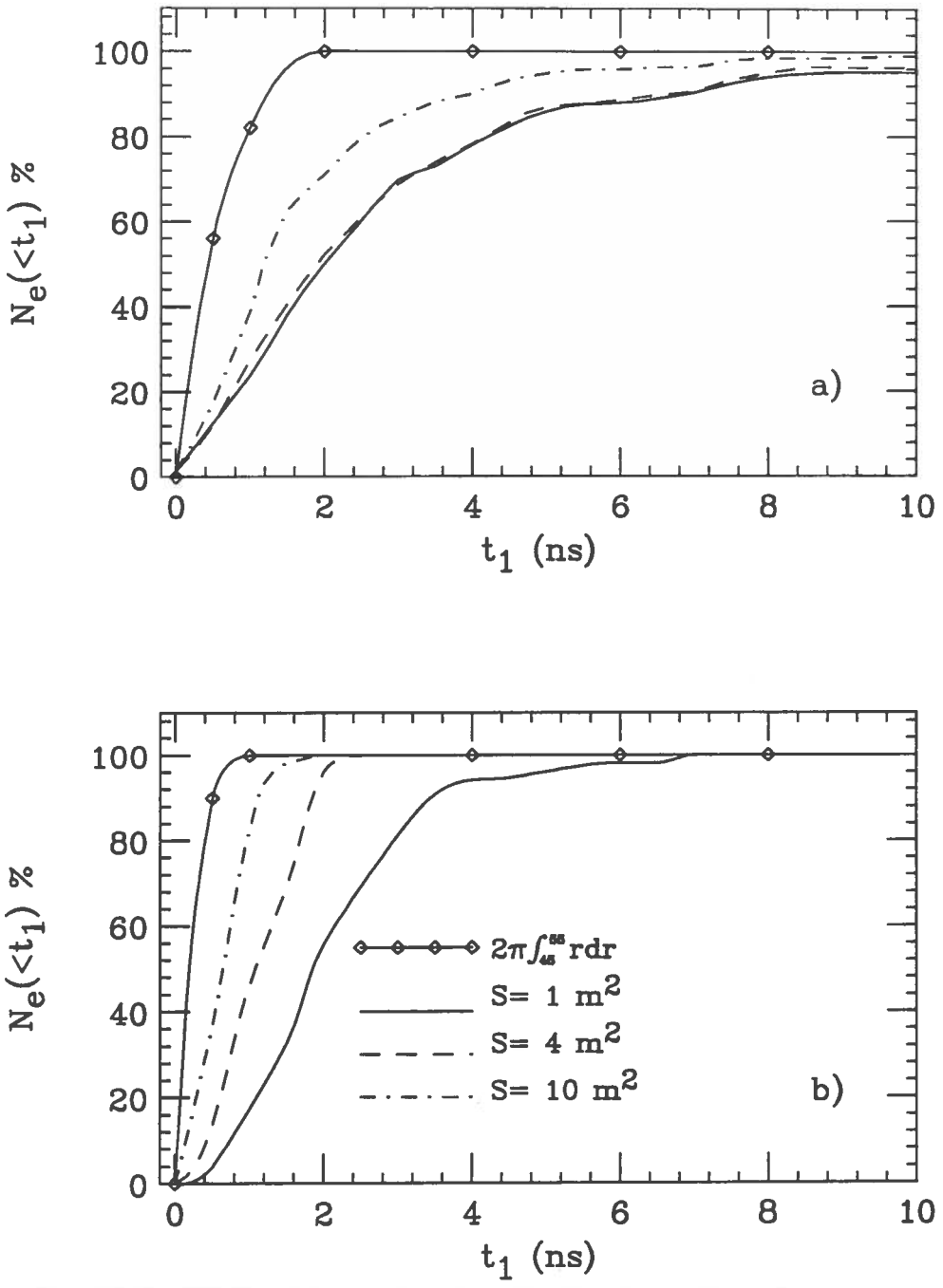
100
80
60
40
20
0
$N_e(<t_1)$ %
0
2
4
6
8
10
t_1 (ns)
a)
b)
$2\pi\int_{48}^{55} rdr$
S= 1 m^2
S= 4 m^2
S= 10 m^2

FIG. 21

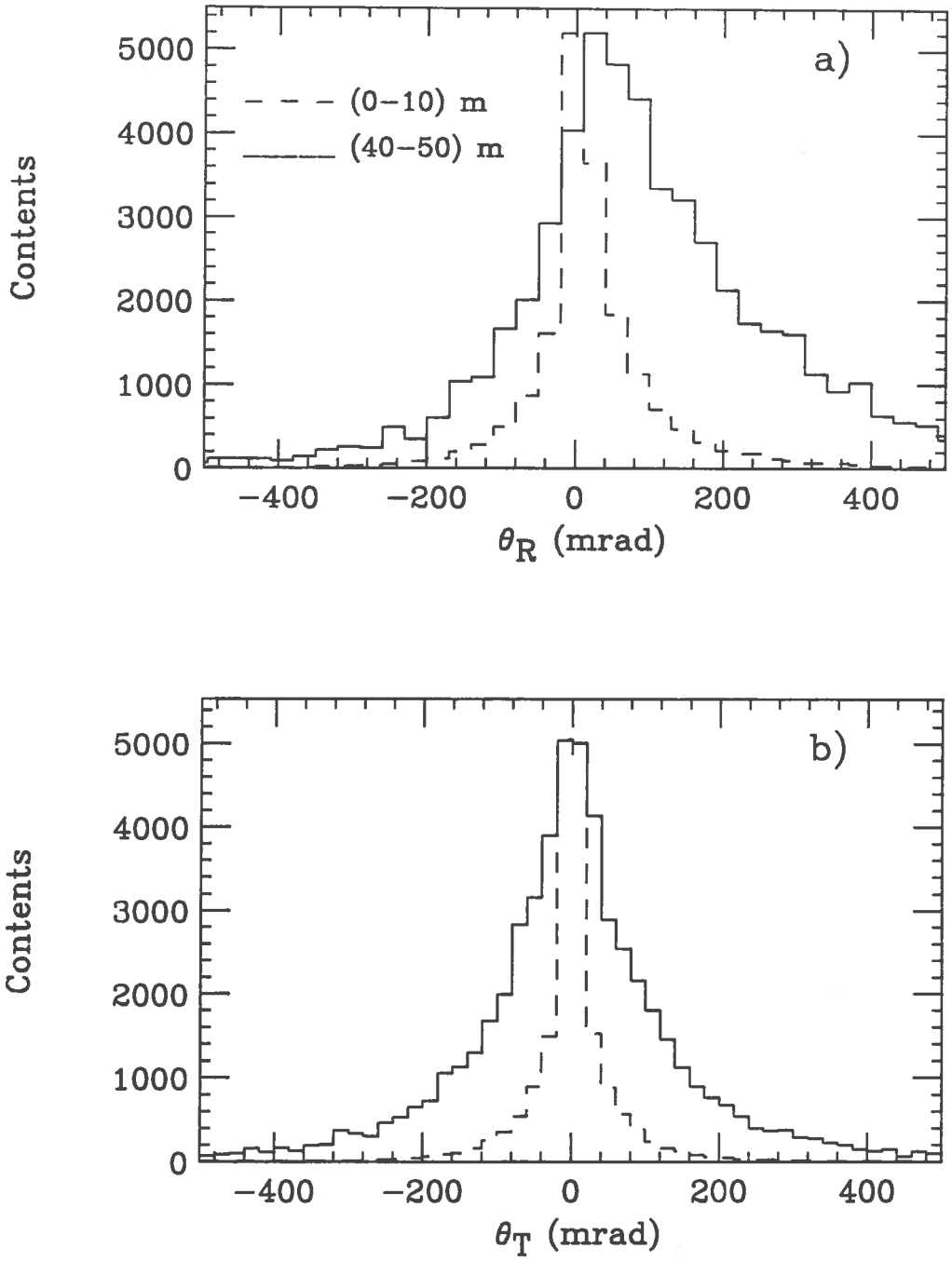
a)
(0–10) m
(40–50) m
Contents
5000
4000
3000
2000
1000
0
−400
−200
0
200
400
θ_R (mrad)
b)
Contents
5000
4000
3000
2000
1000
0
−400
−200
0
200
400
θ_T (mrad)

FIG. 22

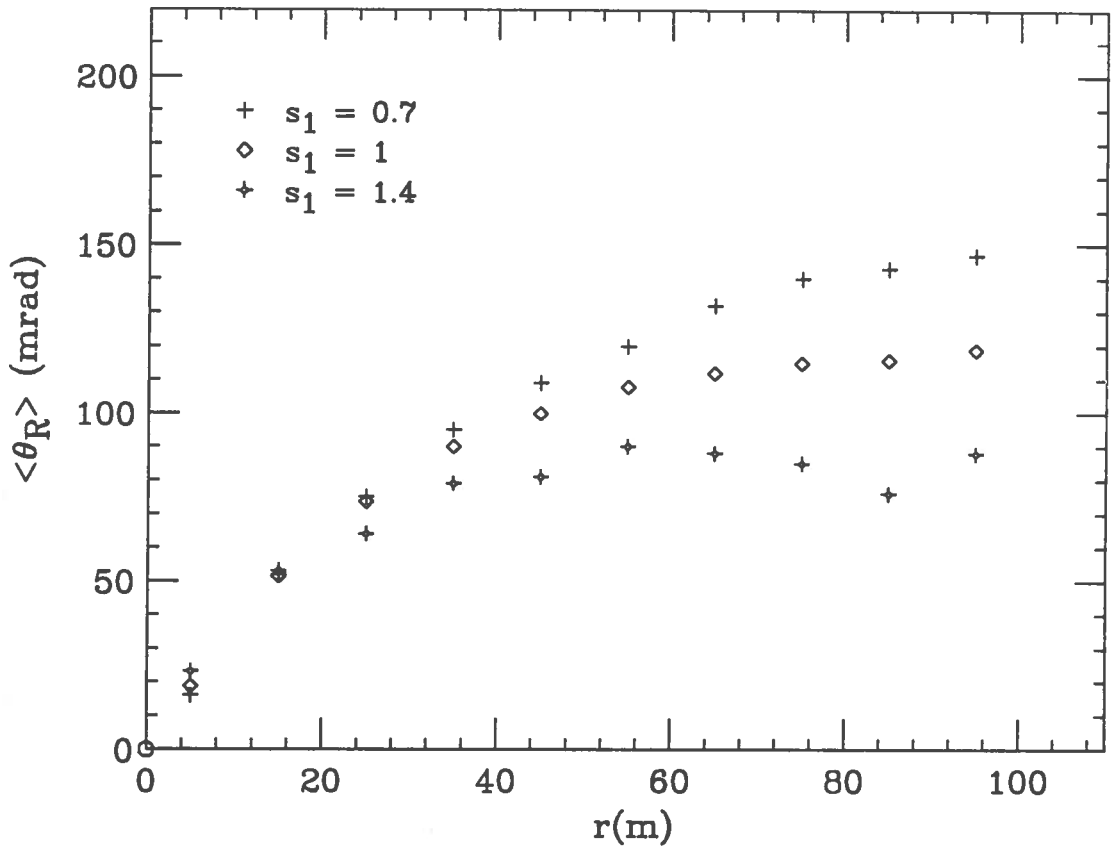

FIG. 23

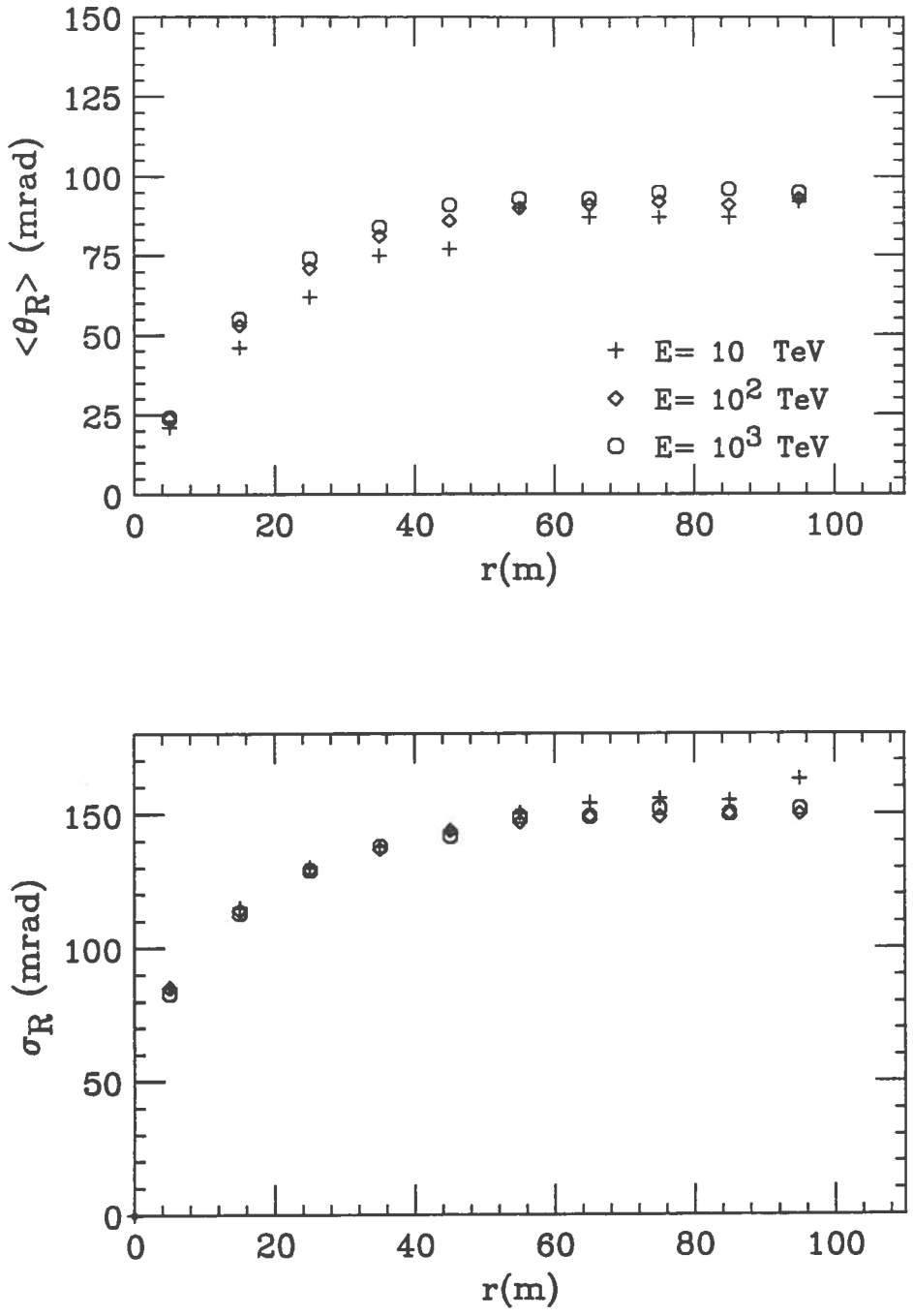
150
125
100
75
50
25
0
$<\theta_R>$ (mrad)
0
20
40
60
80
100
r(m)
+ E= 10 TeV
◇ E= 10^2 TeV
○ E= 10^3 TeV
150
100
50
0
σ_R (mrad)
0
20
40
60
80
100
r(m)

FIG. 24

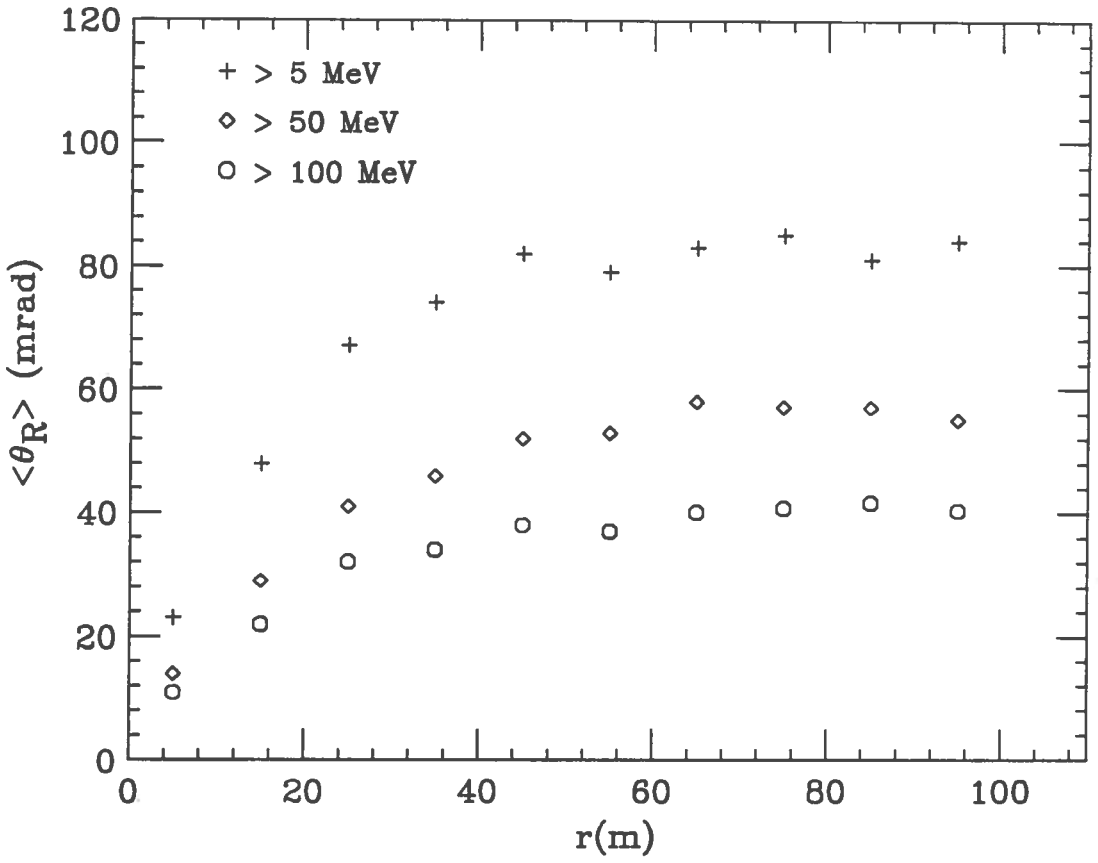

FIG. 25

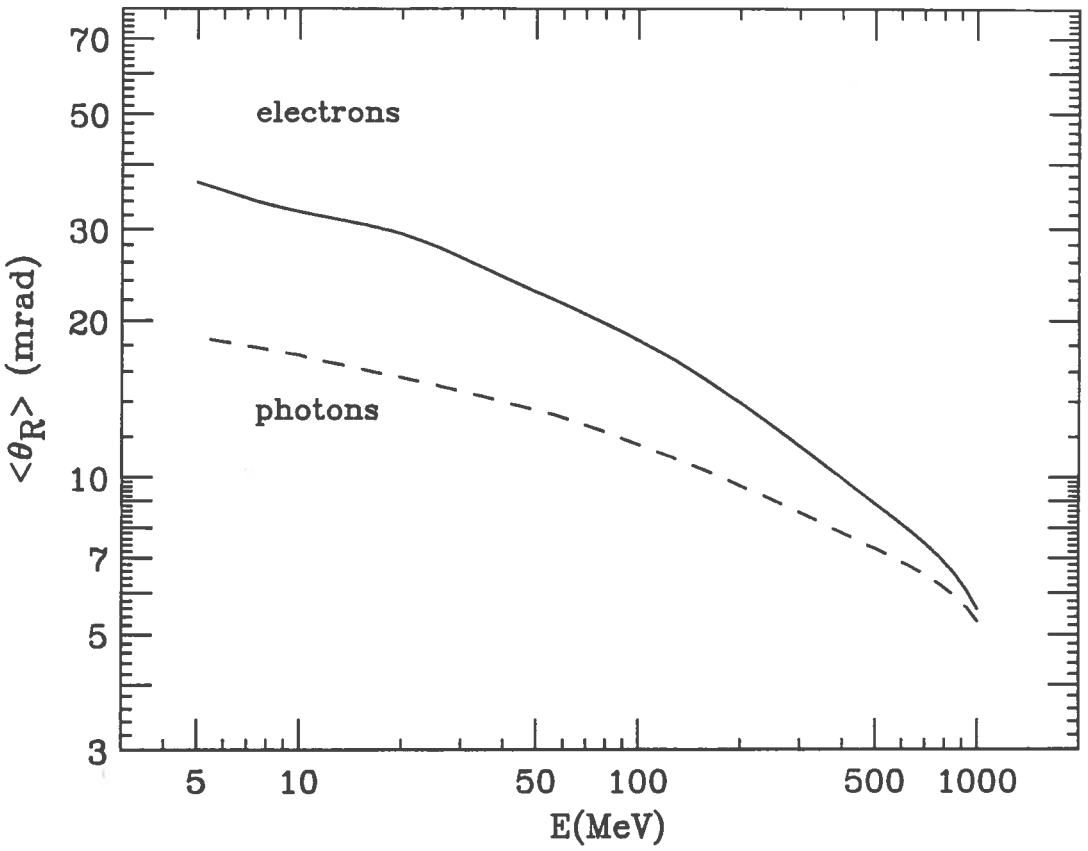
70
50
30
20
10
7
5
3
electrons
photons
<θR> (mrad)
5
10
50
100
500
1000
E(MeV)

FIG. 26